

Enhancement of transmission quality in soliton-based optical waveguide systems by frequency dependent linear gain-loss and the Raman self-frequency shift

Avner Peleg¹, Debananda Chakraborty²

¹ *Department of Exact Sciences, Afeka College of Engineering, Tel Aviv 69988, Israel*

² *Department of Mathematics, New Jersey City University,
Jersey City, New Jersey 07305, USA*

(Dated: November 9, 2018)

Abstract

We study transmission stabilization against radiation emission in soliton-based nonlinear optical waveguides with weak linear gain-loss, cubic loss, and delayed Raman response. We show by numerical simulations with perturbed nonlinear Schrödinger propagation models that transmission quality in waveguides with frequency independent linear gain and cubic loss is not improved by the presence of delayed Raman response due to the lack of an efficient mechanism for suppression of radiation emission. In contrast, we find that the presence of delayed Raman response leads to significant enhancement of transmission quality in waveguides with frequency dependent linear gain-loss and cubic loss. Enhancement of transmission quality in the latter waveguides is enabled by the separation of the soliton's spectrum from the radiation's spectrum due to the Raman-induced self-frequency shift and by efficient suppression of radiation emission due to the frequency dependent linear gain-loss. Further numerical simulations demonstrate that the enhancement of transmission quality in waveguides with frequency dependent linear gain-loss, cubic loss, and delayed Raman response is similar to transmission quality enhancement in waveguides with linear gain, cubic loss, and guiding filters with a varying central frequency.

PACS numbers: 42.65.Tg, 42.81.Dp, 42.65.Dr

I. INTRODUCTION

Transmission of solitons in nonlinear optical waveguide systems has been the subject of intensive research in the last several decades due to the stability and shape preserving properties of the solitons [1–4]. In addition, since Kerr nonlinearity does not cause any pulse distortion in single-soliton propagation, soliton-based transmission can be used to realize higher transmission rates and larger error-free transmission distances compared with other transmission methods [2, 4–7]. This is true for example for transmission in optical fibers. Indeed, in Ref. [8], error-free optical fiber transmission of a single sequence of optical solitons at a bit rate of 10 Gb/s over 10^6 km was experimentally demonstrated by using synchronous modulation. In another experiment, error-free transmission of seven soliton sequences at 10 Gb/s per sequence over transoceanic distances was realized, using dispersion-tapered optical fibers and guiding filters with a varying central frequency [9]. Even larger transmission rates were experimentally demonstrated with dispersion-managed solitons. In particular, in Ref. [7], transmission of 25 sequences of dispersion-managed solitons at 40 Gb/s per sequence over 1500 km was achieved. Furthermore, transmission of 109 dispersion-managed soliton sequences at 10 Gb/s per sequence over 2×10^4 km was demonstrated in Ref. [10].

In the current paper, we study transmission stabilization of conventional optical solitons, that is, of solitons of the cubic nonlinear Schrödinger (NLS) equation without dispersion management. Our reasons for considering conventional optical solitons are the following. First, as stated in the first paragraph, because of the stability and shape-preserving properties of the solitons, soliton-based transmission is advantageous compared with other transmission methods. Second, due to the integrability of the unperturbed cubic NLS equation, derivation of the equations for dynamics of the soliton parameters in the presence of perturbations can be done in a rigorous manner. Third, the simpler properties of conventional solitons compared with dispersion-managed solitons make them more suitable for usage in optical networks and in other optical systems, where simplicity and scalability are important. Fourth, even though the details of pulse dynamics in other transmission systems might be different, analysis of transmission stabilization of conventional optical solitons can still provide a rough idea on how to realize transmission stabilization in other waveguide setups.

In several earlier works, we developed a general method for stabilizing the dynamics of optical soliton amplitudes in multisequence nonlinear optical waveguide systems with weak

nonlinear dissipation [11–18]. The method is based on showing that amplitude dynamics induced by the dissipation in N -sequence optical waveguide systems can be approximately described by N -dimensional Lotka-Volterra (LV) models. Stability analysis of the equilibrium states of the LV models can then be used for realizing stable amplitude dynamics along ultra-long distances. However, due to the instability of multisequence soliton-based transmission against resonant and non-resonant emission of radiation, the distances along which stable amplitude dynamics was observed in numerical simulations with the perturbed NLS equation were initially limited to a few hundred dispersion lengths [12, 13]. Further analysis showed that a major mechanism for transmission destabilization in these systems is associated with resonant emission of radiation during intersequence soliton collisions, where the emitted radiation undergoes unstable growth and develops into radiative sidebands [16, 17, 19]. Significant increase in the stable propagation distances was achieved by the introduction of frequency dependent linear gain-loss in N -waveguide couplers [16–19]. It was shown in these works that the presence of frequency dependent linear gain-loss leads to efficient suppression of the instability due to resonant radiation emission. The limiting cause for transmission instability in N -waveguide couplers with frequency dependent linear gain-loss was associated with non-resonant radiation emission due to the effects of the dissipation on single-soliton propagation [16, 18]. Therefore, the latter process is a serious obstacle for further enhancement of transmission stability in nonlinear optical waveguide systems, where conventional optical solitons are used.

In two of the recent works, where stable long-distance multisequence transmission with conventional solitons was demonstrated, the effects of delayed Raman response were taken into account in addition to the effects of frequency dependent linear gain-loss [16, 17]. The stable transmission distances achieved in these studies were larger by two orders of magnitude compared with the distances obtained in earlier studies, where the effects of frequency dependent linear gain-loss and delayed Raman response were not taken into account [12, 13]. It is known that the most important effect of delayed Raman response on single-soliton propagation in nonlinear optical waveguides is a continuous downshift of the soliton’s frequency, which is called the Raman self-frequency shift [20–22]. In view of the findings in Refs. [16, 17], it is important to investigate whether the combination of frequency dependent linear gain-loss and one of the effects associated with delayed Raman response, such as the Raman self-frequency shift, can indeed lead to significant enhancement of transmission

stability in soliton-based optical waveguide systems. If such transmission stabilization is possible, it is important to characterize the mechanism leading to the stabilization.

In the current paper, we take on these important tasks by studying propagation of a single soliton in nonlinear optical waveguides with weak linear gain-loss, cubic loss, and delayed Raman response. We characterize transmission quality and stability by calculating the transmission quality integral, which measures the deviation of the pulse shape obtained in numerical simulations with perturbed NLS equations from the shape expected by the perturbation theory for the NLS soliton. In addition, we compare the dynamics of the soliton's amplitude and frequency obtained in the simulations with the dynamics expected by the perturbation theory. We first study soliton propagation in the absence of delayed Raman response. Our numerical simulations with the perturbed NLS equations show that transmission quality in waveguides with frequency independent linear gain and cubic loss is comparable to transmission quality in waveguides with frequency dependent linear gain-loss and cubic loss. We then include the effects of delayed Raman response in the perturbed NLS model. Our numerical simulations show that in waveguides with frequency independent linear gain, cubic loss, and delayed Raman response, the soliton's spectrum becomes separated from the radiation's spectrum due to the Raman-induced self-frequency shift experienced by the soliton. However, in this case transmission quality is not improved compared with transmission quality in the absence of delayed Raman response due to the lack of an efficient mechanism for suppression of radiation emission. Furthermore, for waveguides with frequency dependent linear gain-loss, cubic loss, and delayed Raman response, we observe significant enhancement of transmission quality compared with transmission quality in the absence of delayed Raman response. The enhancement of transmission quality in the latter waveguides is enabled by the separation of the soliton's spectrum from the radiation's spectrum due to the Raman self-frequency shift and by the efficient suppression of radiation emission due to the frequency dependent linear gain-loss. Additionally, we show by further numerical simulations that enhancement of transmission quality in waveguides with frequency dependent linear gain-loss, cubic loss, and delayed Raman response is similar to transmission quality enhancement in waveguides with weak linear gain, cubic loss, and guiding filters with a varying central frequency. More specifically, we demonstrate that the variation of the central filtering frequency leads to separation of the soliton's spectrum from the radiation's spectrum, while the presence of the guiding filters leads to efficient

suppression of radiation emission.

We choose to study pulse propagation in optical waveguides with linear gain or loss and cubic loss as a major example for waveguides, in which linear and nonlinear dissipation plays an important role in pulse dynamics. The waveguide's cubic loss can arise due to two-photon absorption (2PA) or gain/loss saturation [23–26]. Pulse propagation in the presence of 2PA or cubic loss has been studied in many previous works [12, 27–36]. The subject received further attention in recent years due to the importance of 2PA in silicon nanowaveguides, which are expected to play a key role in many applications in optoelectronic devices [24, 25, 37, 38]. These applications include modulators [39, 40], switches [41, 42], regeneration [43], pulse compression [44], logical gates [45, 46], and supercontinuum generation [47]. In many of the applications it is desired to achieve a steady state, in which the pulse propagates along the waveguide with a constant amplitude. This can be realized by providing linear gain via Raman amplification [48–52]. We also point out that it was recently demonstrated that waveguide spans with linear gain and cubic loss can be used for robust transmission switching and transmission recovery in hybrid soliton-based nonlinear waveguide systems [15, 17].

The rest of the paper is organized as follows. In Section II, we study transmission stabilization in waveguides with linear gain or loss and cubic loss, considering frequency independent linear gain in Section II A and frequency dependent linear gain-loss in Section II B. In Section III, we investigate transmission stabilization in waveguides with linear gain or loss, cubic loss, and delayed Raman response. We consider frequency independent linear gain in Section III A and frequency dependent linear gain-loss in Section III B. In Section IV, we study transmission stabilization in waveguides with linear gain, cubic loss, and guiding optical filters, considering a constant central filtering frequency in Section IV A and a varying central filtering frequency in Section IV B. Our conclusions are summarized in Section V. In A, we present a brief summary of the adiabatic perturbation theory for the NLS soliton. In B, we describe the calculation of the transmission quality integral, while in C, we derive the equation for dynamics of the soliton's amplitude in the presence of frequency dependent linear gain-loss.

II. PULSE DYNAMICS IN WAVEGUIDES WITH LINEAR GAIN-LOSS AND CUBIC LOSS

A. Waveguides with frequency independent linear gain and cubic loss

We consider propagation of an optical pulse in a nonlinear optical waveguide in the presence of second-order dispersion, Kerr nonlinearity, weak frequency independent linear gain, and weak cubic loss. The frequency independent linear gain can be realized by distributed Raman amplification [48, 49]. The propagation is described by the following perturbed NLS equation [24, 25, 29]:

$$i\partial_z\psi + \partial_t^2\psi + 2|\psi|^2\psi = ig_0\psi/2 - i\epsilon_3|\psi|^2\psi, \quad (1)$$

where ψ is proportional to the envelope of the electric field, z is propagation distance, t is time, and g_0 and ϵ_3 are the linear gain and cubic loss coefficients [53]. These coefficients satisfy $0 < g_0 \ll 1$ and $0 < \epsilon_3 \ll 1$. The second and third terms on the left-hand side of Eq. (1) are due to second-order dispersion and Kerr nonlinearity, while the first and second terms on the right-hand side of Eq. (1) are due to linear gain and cubic loss. In the current paper we study transmission stabilization for fundamental solitons of the unperturbed NLS equation. The envelope of the electric field for these solitons is given by:

$$\psi_s(t, z) = \eta \exp(i\chi) / \cosh(x), \quad (2)$$

where $x = \eta(t - y + 2\beta z)$, $\chi = \alpha - \beta(t - y) + (\eta^2 - \beta^2)z$, and η , β , y , and α are the soliton amplitude, frequency, position, and phase.

The equations for the dynamics of the soliton amplitude and frequency are obtained by using the adiabatic perturbation theory for the NLS soliton, see, e.g., Refs. [3, 54–56] and A. In the case of soliton propagation in the presence of linear gain and cubic loss, we obtain:

$$\frac{d\eta}{dz} = g_0\eta - \frac{4}{3}\epsilon_3\eta^3, \quad (3)$$

and $d\beta/dz = 0$. Since we are interested in realizing stable transmission of the soliton with a constant amplitude, we require that $\eta = \eta_0 > 0$ is an equilibrium point of Eq. (3). This requirement yields $g_0 = 4\eta_0^2/3$. Thus, the equation for amplitude dynamics is:

$$\frac{d\eta}{dz} = \frac{4}{3}\epsilon_3\eta(\eta_0^2 - \eta^2). \quad (4)$$

The solution of this equation for a soliton with an initial amplitude $\eta(0)$ is

$$\eta(z) = \eta_0 \left[1 + \left(\frac{\eta_0^2}{\eta^2(0)} - 1 \right) \exp(-8\eta_0^2 \epsilon_3 z / 3) \right]^{-\frac{1}{2}}. \quad (5)$$

It is clear from both Eqs. (4) and (5) that the equilibrium point at $\eta = \eta_0$ is stable, while the one at $\eta = 0$ is unstable.

Numerical simulations. The prediction for stable dynamics of the soliton amplitude that was obtained in the previous paragraph was based on an adiabatic perturbation description, which neglects the effects of radiation emission. However, radiation emission effects can become significant at large propagation distances and this can lead to pulse shape distortion and to the breakdown of the adiabatic perturbation description of Eqs. (4) and (5). This is especially true in waveguides with linear gain, since the presence of linear gain leads to unstable growth of small amplitude waves that are associated with radiation. It is therefore important to check the predictions obtained with the adiabatic perturbation theory by numerical simulations with the perturbed NLS model (1).

Equation (1) is numerically integrated on a domain $[t_{\min}, t_{\max}] = [-1600, 1600]$ using the split-step method with periodic boundary conditions [1, 57]. The initial condition is in the form of a single NLS soliton ψ_s with amplitude $\eta(0)$, frequency $\beta(0) = 0$, position $y(0) = 0$, and phase $\alpha(0) = 0$. For concreteness, we present here the results of numerical simulations with $\epsilon_3 = 0.01$ and $\eta(0) = 0.8$. We emphasize, however, that similar results are obtained for other values of the physical parameters. To avoid dealing with effects due to radiation leaving the computational domain at one boundary and re-entering it at the other boundary, we employ damping near the domain boundaries. The same method for suppressing re-entry of radiation into the computational domain was successfully used in many earlier studies of pulse propagation in nonlinear optical waveguides, see, e.g., Refs. [35, 58, 59]. Physically, the damping at the boundaries can be realized by employing filters at the waveguide ends [1, 2]. Thus, the numerical simulations in the current section correspond to transmission in an open optical waveguide.

Transmission quality at a distance z is measured from the results of the numerical simulations by calculating the transmission quality integral $I(z)$ in Eq. (B4) in B. This integral measures the deviation of the numerically obtained pulse shape $|\psi^{(num)}(t, z)|$ from the soliton's shape expected by the adiabatic perturbation theory $|\psi^{(th)}(t, z)|$, which is given by Eq. (B1). Thus, $I(z)$ measures both distortion in the pulse shape due to radiation emission and

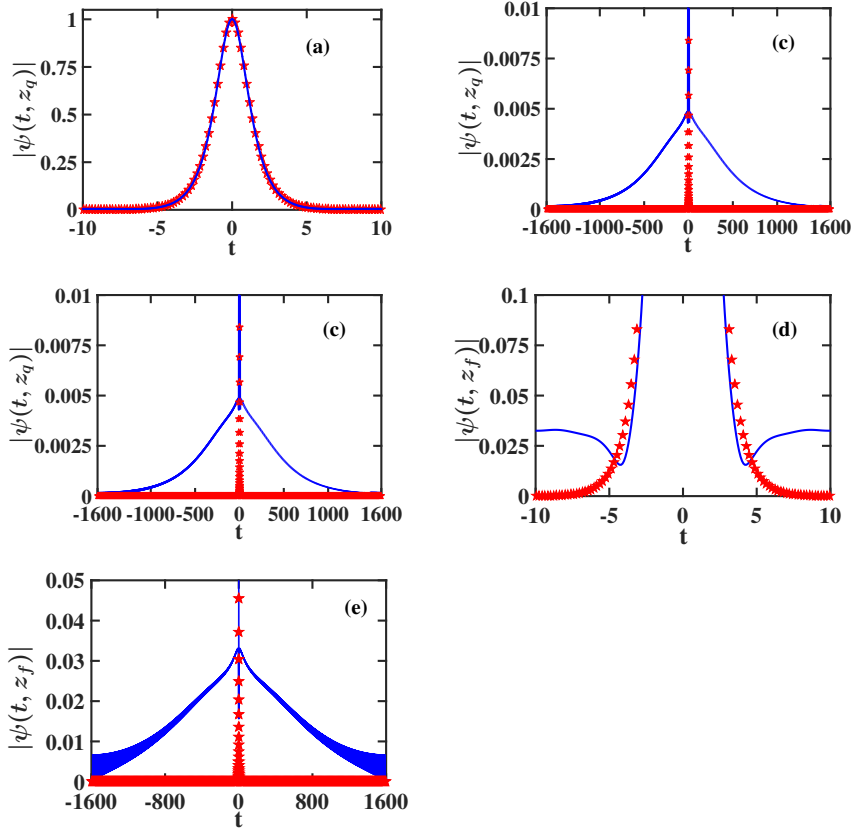


FIG. 1: The pulse shape $|\psi(t, z)|$ at $z_q = 432$ [(a), (b), and (c)] and at $z_f = 750$ [(d) and (e)] for soliton propagation in an open optical waveguide with weak frequency independent linear gain and cubic loss. The cubic loss coefficient is $\epsilon_3 = 0.01$ and the initial soliton amplitude is $\eta(0) = 0.8$. The solid blue curve corresponds to the result obtained by numerical simulations with Eq. (1), while the red stars correspond to the perturbation theory prediction of Eqs. (B1) and (5).

deviations in the numerically obtained values of the soliton's parameters from the values predicted by the adiabatic perturbation theory. Transmission quality is further quantified by measuring the transmission quality distance z_q , which is the distance at which the value of $I(z)$ first exceeds 0.075. In the numerical simulation with $\epsilon_3 = 0.01$ and $\eta(0) = 0.8$ we find $z_q = 432$. To characterize pulse shape degradation at larger distances, we run the simulation up to a final propagation distance z_f at which the value of $I(z)$ first exceeds 0.655. In the simulation with $\epsilon_3 = 0.01$ and $\eta(0) = 0.8$ we find $z_f = 750$.

Figure 1 shows the pulse shape $|\psi(t, z)|$ at $z = z_q$ and at $z = z_f$, as obtained by the numerical simulations. Also shown is the analytic prediction of Eqs. (B1) and (5), which is obtained by the adiabatic perturbation theory. As seen in Figs. 1(a) and 1(b), the pulse

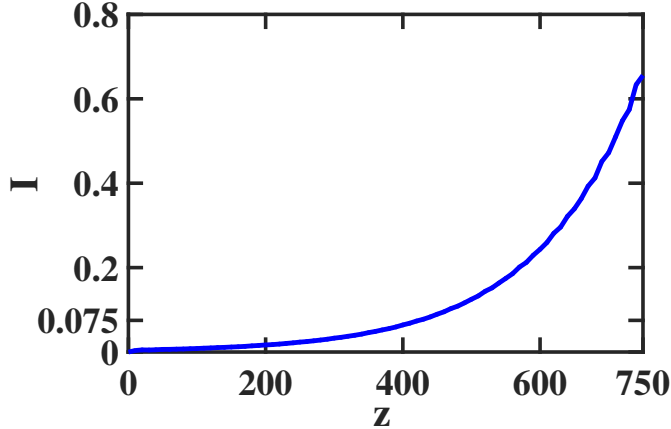


FIG. 2: The z dependence of the transmission quality integral $I(z)$ obtained by numerical simulations with Eq. (1) for the same optical waveguide setup considered in Fig. 1.

shape obtained by the simulations at $z = z_q$ is close to the analytic prediction. However, the comparison of the analytic prediction with the numerical result for small $|\psi(t, z_q)|$ values in Fig. 1(c) reveals that an appreciable radiative tail exists already at $z = z_q$. As the soliton continues to propagate along the waveguide the radiative tail continues to grow [see Figs. 1(d) and 1(e)]. The growth of the radiative tail is also manifested in Fig. 2, which shows the values of the integral $I(z)$ obtained in the simulations. As seen in this figure, the value of $I(z)$ increases from 0.075 at $z_q = 432$ to 0.6556 at $z_f = 750$.

The growth of the radiative tail can be further characterized by the shape of the Fourier transform of the pulse $|\hat{\psi}(\omega, z)|$. Figure 3 shows the Fourier transform $|\hat{\psi}(\omega, z)|$ at $z = z_q$ and at $z = z_f$, as obtained by the numerical simulations. Also shown is the prediction of the adiabatic perturbation theory, obtained with Eqs. (B3) and (5). As seen in Figs. 3(a) and 3(b), the deviation of the numerical result from the analytic prediction is noticeable already at $z = z_q$. This deviation appears as fast oscillations in the numerical curve of $|\hat{\psi}(\omega, z)|$, which are most pronounced near $\omega = 0$, i.e., at relatively small frequencies. Furthermore, the difference between the numerical result and the analytic prediction continues to grow as the pulse continues to propagate along the waveguide. Indeed, as seen in Fig. 3(c), the difference between the analytic prediction and the numerical result at $z = z_f$ is already of order 1.

The z dependence of the soliton amplitude obtained in the simulations is shown in Fig. 4 along with the analytic prediction of Eq. (5). We observe good agreement between the

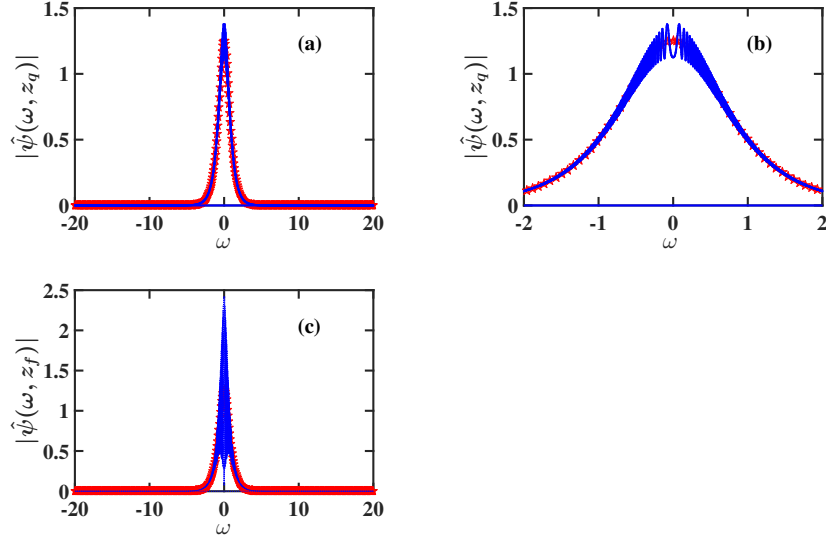


FIG. 3: The Fourier transform of the pulse shape $|\hat{\psi}(\omega, z)|$ at $z_q = 432$ [(a) and (b)] and at $z_f = 750$ (c) for soliton propagation in an open optical waveguide with weak frequency independent linear gain and cubic loss. The physical parameter values are the same as in Fig. 1. The solid blue curve represents the result obtained by numerical simulations with Eq. (1), while the red stars correspond to the prediction of the adiabatic perturbation theory, obtained with Eqs. (B3) and (5).

numerical and analytic results for $0 \leq z \leq 600$. For $600 < z \leq 750$, the difference between the numerical result and the analytic prediction becomes noticeable. The good agreement between the analytic prediction and the numerical result for $\eta(z)$ can be attributed to the fact that radiation emission affects the dynamics of η only in second order of the small perturbation parameter ϵ_3 (see, e.g., Refs. [55, 56]).

We emphasize that the effects of radiation emission due to weak perturbations can have much stronger impact on soliton dynamics and stability compared with the impact observed here for single-soliton propagation in an open optical waveguide. More specifically, in the case of transmission of a soliton sequence through an optical waveguide, the emitted radiation leads to long-range interaction between the solitons, which in turn leads to the breakup of the soliton pattern [56]. Furthermore, in the case of transmission of multiple soliton sequences through an optical waveguide, the radiation emitted by the solitons in a given sequence can resonantly interact with solitons from other sequences [16, 17, 19]. This resonant interaction leads to severe pulse pattern distortion and eventually to the destruction of the soliton

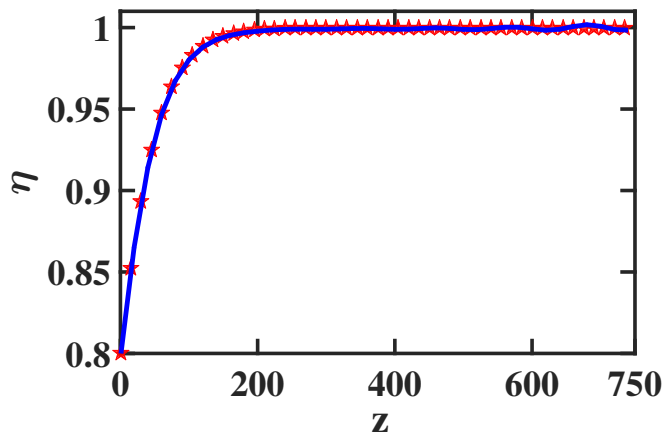


FIG. 4: The z dependence of the soliton amplitude $\eta(z)$ for the open waveguide setup considered in Figs. 1-3. The solid blue curve represents the result obtained by numerical simulations with Eq. (1). The red stars represent the perturbation theory prediction of Eq. (5).

sequences [12, 13, 16, 17, 19]. Finally, in the case of a soliton propagating in a closed waveguide loop, the accumulation of the emitted radiation and its interaction with the soliton will also lead to pulse shape distortion and to the destruction of the soliton. This latter scenario will be discussed and demonstrated in sections 3 and 4.

B. Waveguides with frequency dependent linear gain-loss and cubic loss

As seen in section II A, transmission quality in a waveguide with frequency independent linear gain and cubic loss is degraded at relatively short distances due to radiation emission. It is therefore important to look for waveguide setups, in which radiation emission might be suppressed. A possible way for achieving this goal is by employing frequency dependent linear gain-loss, such that the weak effects of cubic loss are balanced by weak linear gain in a frequency interval centered around the soliton frequency, while radiation emission effects are mitigated by relatively strong linear loss outside this frequency interval [16–19]. Indeed, it was shown in several recent works that the implementation of such frequency dependent linear gain-loss can lead to significant enhancement of transmission stability in *multisequence* soliton-based optical waveguide systems [16–19]. We therefore turn to investigate soliton propagation in the presence of frequency dependent linear gain-loss and weak cubic loss.

The propagation is described by the perturbed NLS equation [17, 18]

$$i\partial_z\psi + \partial_t^2\psi + 2|\psi|^2\psi = i\mathcal{F}^{-1}(\hat{g}(\omega)\hat{\psi})/2 - i\epsilon_3|\psi|^2\psi, \quad (6)$$

where ω is frequency, $\hat{\psi}$ is the Fourier transform of ψ with respect to time, $\hat{g}(\omega)$ is the frequency dependent linear gain-loss, and \mathcal{F}^{-1} is the inverse Fourier transform with respect to time.

The form of $\hat{g}(\omega)$ is chosen such that radiation emission effects are mitigated, while the soliton amplitude still approaches η_0 with increasing propagation distance. In particular, we choose the form [19]:

$$\begin{aligned} \hat{g}(\omega) = & -g_L + \frac{1}{2}(g_0 + g_L) [\tanh\{\rho[\omega + \beta(0) + W/2]\} \\ & - \tanh\{\rho[\omega + \beta(0) - W/2]\}], \end{aligned} \quad (7)$$

where $\beta(0)$ is the initial soliton frequency, g_L is an $O(1)$ positive constant, and the constants W and ρ satisfy $W \gg 1$ and $\rho \gg 1$. In the limit $\rho \gg 1$, the linear gain-loss $\hat{g}(\omega)$ can be approximated by a step function, which is equal to g_0 inside a frequency interval of width W centered about $-\beta(0)$, and to $-g_L$ elsewhere:

$$\hat{g}(\omega) \simeq \begin{cases} g_0 & \text{if } -\beta(0) - W/2 < \omega \leq -\beta(0) + W/2, \\ -g_L & \text{elsewhere.} \end{cases} \quad (8)$$

The potential advantages of using the frequency dependent linear gain-loss function (7) can be explained with the help of the approximate expression (8). The weak linear gain g_0 in the frequency interval $(-\beta(0) - W/2, -\beta(0) + W/2]$ balances the effects of cubic loss, such that the soliton amplitude tends to η_0 with increasing z . The relatively strong linear loss g_L leads to suppression of emission of radiation with frequencies outside of the interval $(-\beta(0) - W/2, -\beta(0) + W/2]$. The flat gain in the interval $(-\beta(0) - W/2, -\beta(0) + W/2]$ can be realized by flat-gain amplifiers [60], and the strong loss outside of this interval can be achieved by filters [60] or by waveguide impurities [1].

In C, we show that within the framework of the adiabatic perturbation theory, the dynamics of the soliton amplitude is described by

$$\frac{d\eta}{dz} = [-g_L + (g_0 + g_L) \tanh(V) - 4\epsilon_3\eta^2/3] \eta, \quad (9)$$

where $V = \pi W/(4\eta)$. To realize stable transmission with a constant amplitude $\eta_0 > 0$, we require that $\eta = \eta_0 > 0$ is a stable equilibrium point of Eq. (9). This requirement yields

$$g_0 = g_L \left[\frac{1}{\tanh(V_0)} - 1 \right] + \frac{4\epsilon_3\eta_0^2}{3 \tanh(V_0)}, \quad (10)$$

where $V_0 = \pi W/(4\eta_0)$. Substituting Eq. (10) into Eq. (9), we obtain:

$$\frac{d\eta}{dz} = \eta \left\{ g_L \left[\frac{\tanh(V)}{\tanh(V_0)} - 1 \right] + \frac{4}{3}\epsilon_3 \left[\eta_0^2 \frac{\tanh(V)}{\tanh(V_0)} - \eta^2 \right] \right\}. \quad (11)$$

In C, we show that the only equilibrium points of Eq. (11) with $\eta \geq 0$ are $\eta = \eta_0$ and $\eta = 0$. In addition, we show that $\eta = \eta_0$ is a stable equilibrium point, while $\eta = 0$ is an unstable equilibrium point. Thus, the number, locations, and stability properties of the equilibrium points of Eq. (11) and Eq. (4) are the same. In other words, the introduction of the frequency dependent linear gain-loss does not change the equilibrium points properties. We also note that in the typical transmission setup that we consider in the current work, η_0 is of order 1, η is of order 1 or smaller, and $W \gg 1$ [61]. Therefore, in this case both V_0 and V satisfy $V_0 \gg 1$ and $V \gg 1$, and one can obtain an approximate form of Eq. (11) by expanding its right hand side in a Taylor series with respect to e^{-2V_0} and e^{-2V} . Keeping terms up to first order in the expansion, we obtain:

$$\begin{aligned} \frac{d\eta}{dz} = & \left[2g_L (e^{-2V_0} - e^{-2V}) + \frac{4}{3}\epsilon_3 (\eta_0^2 - \eta^2) \right. \\ & \left. + \frac{8}{3}\epsilon_3\eta_0^2 (e^{-2V_0} - e^{-2V}) \right] \eta. \end{aligned} \quad (12)$$

Comparing Eq. (12) with Eq. (4) we see that in the typical transmission setup, the correction terms that appear in the equation for amplitude dynamics due to the introduction of frequency dependent linear gain-loss are exponentially small in both V_0 and V .

Numerical simulations. To check whether the introduction of frequency dependent linear gain-loss leads to enhanced transmission stability, we carry out numerical simulations with Eq. (6) and the linear gain-loss (7). The equation is solved on a domain $[t_{\min}, t_{\max}] = [-1600, 1600]$ with periodic boundary conditions and with the same damping at the boundaries as in subsection II A. Therefore, the numerical simulations correspond to open waveguide transmission. The initial condition is in the form of a single NLS soliton with amplitude $\eta(0)$, frequency $\beta(0) = 0$, position $y(0) = 0$, and phase $\alpha(0) = 0$. To enable comparison with the results of numerical simulations for transmission in the presence

of frequency independent linear gain, we use the same parameter values that were used in subsection II A: $\epsilon_3 = 0.01$ and $\eta(0) = 0.8$. In addition, the values of the parameters W , ρ , and g_L of the frequency dependent linear gain-loss $\hat{g}(\omega)$ are similar to the values used in Refs. [16–19] in studies of multisequence soliton-based transmission: $W = 10$, $\rho = 10$, and $g_L = 0.5$. These values were found to lead to enhanced stability of soliton propagation in multisequence transmission systems [16–19]. The values of the transmission quality distance and the final propagation distance obtained in the simulations were $z_q = 432$ and $z_f = 750$, which are the same as the values found for waveguides with frequency independent linear gain.

The pulse shape $|\psi(t, z)|$ obtained in the simulations at $z = z_q$ and at $z = z_f$ is shown in Fig. 5. Also shown is the prediction of the adiabatic perturbation theory, obtained with Eqs. (B1) and (11). We observe that the evolution of the pulse shape is very similar to the one obtained for waveguides with frequency independent linear gain. More specifically, the numerical result for the pulse shape at $z = z_q$ is very close to the prediction of the adiabatic perturbation theory [see Figs. 5(a) and 5(b)]. However, as seen in Fig. 5(c), the soliton develops an appreciable radiative tail at $z = z_q$ with a shape that is very similar to the one observed for waveguides with frequency independent linear gain. Additionally, as seen in Figs. 5(d) and 5(e), the radiative tail keeps growing as the soliton continues to propagate along the waveguide. The growth of the radiative tail with increasing z leads to an increase of the integral $I(z)$ with values that are very close to the values obtained for waveguides with frequency independent linear gain. Indeed, as seen in Fig. 6, the value of $I(z)$ for a waveguide with frequency dependent linear gain-loss increases from 0.075 at $z_q = 432$ to 0.6557 at $z_f = 750$, compared with an increase from 0.075 at $z_q = 432$ to 0.6556 at $z_f = 750$ for a waveguide with frequency independent linear gain.

The similarity between pulse dynamics in the presence of frequency dependent linear gain-loss and frequency independent linear gain can be understood with the help of the Fourier transform of the pulse $|\hat{\psi}(\omega, z)|$. Figure 7 shows the numerically obtained $|\hat{\psi}(\omega, z)|$ at $z = z_q$ and at $z = z_f$ along with the prediction of the adiabatic perturbation theory, obtained with Eqs. (B3) and (11). We observe that the graphs of $|\hat{\psi}(\omega, z_q)|$ and $|\hat{\psi}(\omega, z_f)|$ vs ω are very similar to the graphs obtained for waveguides with frequency independent linear gain. More specifically, the deviation of the numerical result from the analytic prediction is noticeable already at $z = z_q$ and is of order 1 at $z = z_f$. Additionally, the deviation appears as

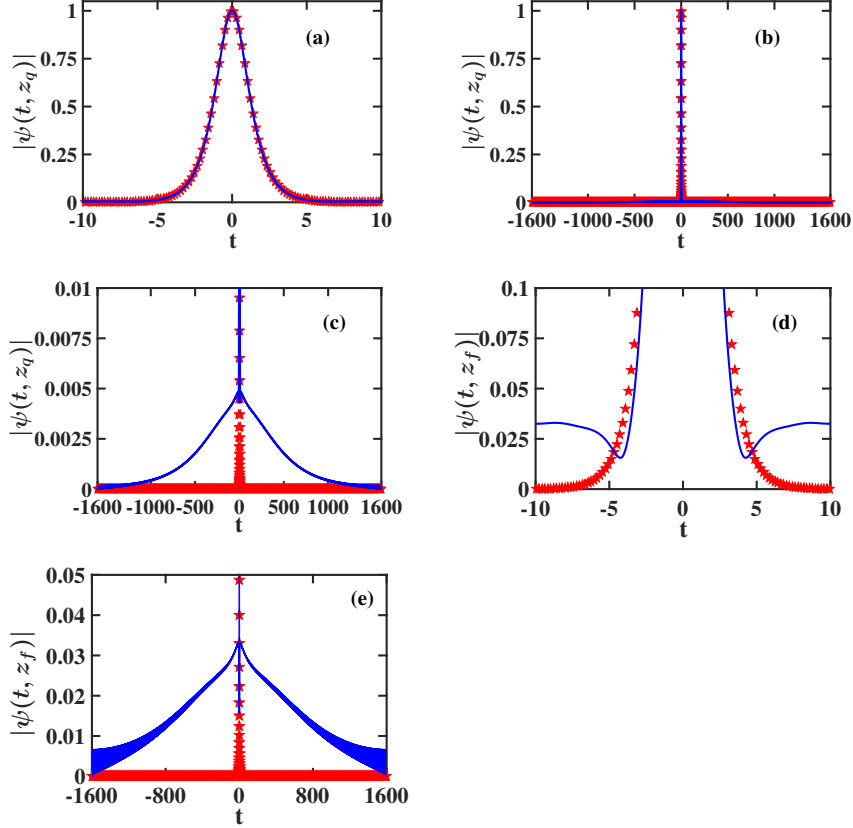


FIG. 5: The pulse shape $|\psi(t, z)|$ at $z_q = 432$ [(a), (b), and (c)] and at $z_f = 750$ [(d) and (e)] for soliton propagation in an open optical waveguide with weak frequency dependent linear gain-loss and cubic loss. The cubic loss coefficient is $\epsilon_3 = 0.01$, the initial soliton amplitude is $\eta(0) = 0.8$, and the parameters of the linear gain-loss $\hat{g}(\omega)$ in Eq. (7) are $W = 10$, $\rho = 10$, and $g_L = 0.5$. The solid blue curve corresponds to the result obtained by numerical simulations with Eqs. (6) and (7), while the red stars correspond to the prediction of the perturbation theory, obtained with Eqs. (B1) and (11).

fast oscillations in the graph of the numerically obtained $|\hat{\psi}(\omega, z)|$ vs ω , which are most pronounced at small ω values. Moreover, there is no observable separation between the Fourier spectrum of the soliton and the Fourier spectrum of the radiation. As a result, the introduction of the frequency dependent linear gain-loss with W values satisfying $W \gg 1$ does not lead to efficient mitigation of radiation emission in the current waveguide setup. We will demonstrate in sections III B and IV B that the situation changes dramatically due to the effects of delayed Raman response or due to the effects of guiding optical filters with a varying central frequency.

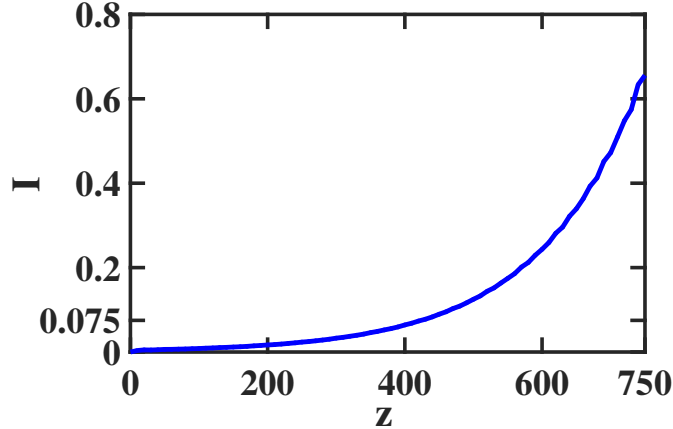


FIG. 6: The z dependence of the transmission quality integral $I(z)$ obtained by numerical simulations with Eqs. (6) and (7) for the same optical waveguide setup considered in Fig. 5.

Figure 8 shows the z dependence of the soliton amplitude obtained in the simulations together with the analytic prediction of Eq. (11). We observe good agreement between the numerical and analytic results for $0 \leq z \leq 600$, while for $600 < z \leq 750$, the difference between the numerical result and the analytic prediction becomes noticeable. Thus, similar to the situation in open optical waveguides with frequency independent linear gain, the dynamics of the soliton amplitude is still stable in the interval $0 \leq z \leq 750$.

III. PULSE DYNAMICS IN WAVEGUIDES WITH LINEAR GAIN-LOSS, CUBIC LOSS, AND DELAYED RAMAN RESPONSE

Introduction. As seen in section II B, the replacement of frequency independent linear gain by frequency dependent linear gain-loss does not lead to significant enhancement of transmission quality. On the other hand, numerical simulations of multisequence soliton-based transmission show that transmission stability is significantly enhanced when the effects of delayed Raman response and frequency dependent linear gain-loss are both taken into account [16, 17]. It is therefore important to investigate whether the presence of delayed Raman response can improve transmission quality in the single-soliton propagation problem considered in the current paper. We now turn to address this question.

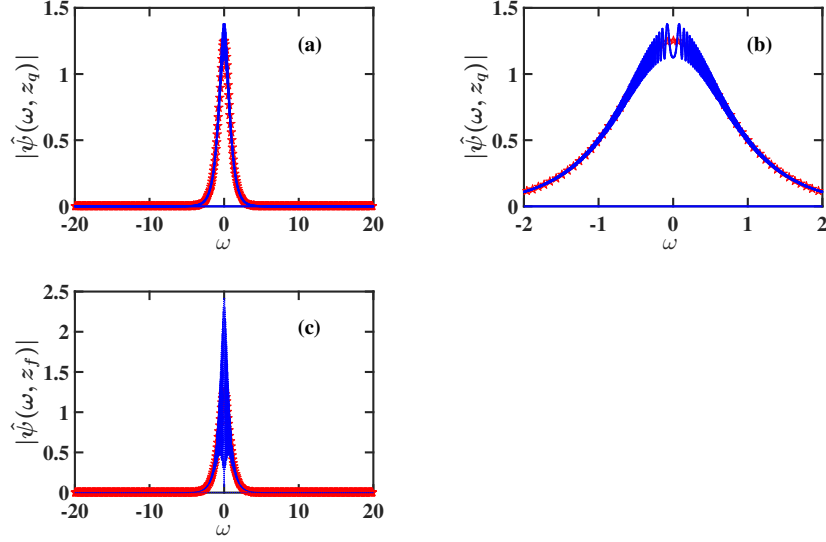


FIG. 7: The Fourier transform of the pulse shape $|\hat{\psi}(\omega, z)|$ at $z_q = 432$ [(a) and (b)] and at $z_f = 750$ (c) for soliton propagation in an open optical waveguide with weak frequency dependent linear gain-loss and cubic loss. The physical parameter values are the same as in Fig. 5. The solid blue curve represents the result obtained by numerical simulations with Eqs. (6) and (7), while the red stars correspond to the prediction of the adiabatic perturbation theory, obtained with Eqs. (B3) and (11).

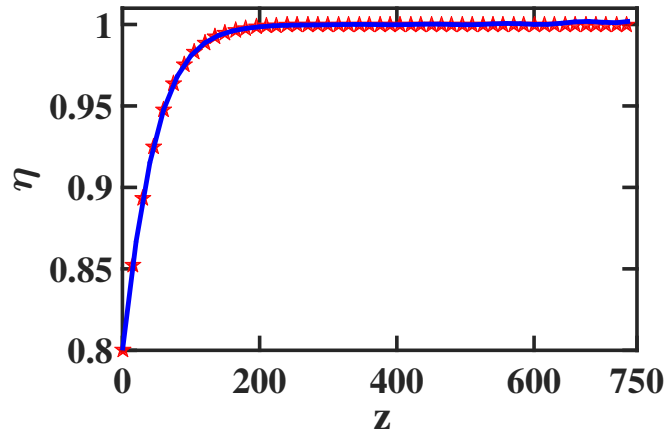


FIG. 8: The z dependence of the soliton amplitude $\eta(z)$ for the open waveguide setup considered in Figs. 5-7. The solid blue curve represents the result obtained by numerical simulations with Eqs. (6) and (7). The red stars represent the perturbation theory prediction of Eq. (11).

A. Waveguides with frequency independent linear gain, cubic loss, and delayed Raman response

We start by considering the impact of delayed Raman response on the propagation of a single soliton in nonlinear optical waveguides with weak frequency independent linear gain and cubic loss. The propagation is described by the following perturbed NLS equation [24, 25]:

$$i\partial_z\psi + \partial_t^2\psi + 2|\psi|^2\psi = ig_0\psi/2 - i\epsilon_3|\psi|^2\psi + \epsilon_R\psi\partial_t|\psi|^2, \quad (13)$$

where the Raman coefficient ϵ_R satisfies $0 < \epsilon_R \ll 1$ [62, 63]. The third term on the right-hand side of Eq. (13) describes the effects of delayed Raman response.

A calculation based on the adiabatic perturbation theory shows that the main effect of delayed Raman response on single-soliton propagation is a frequency shift, whose rate is given by [20–22]:

$$\frac{d\beta}{dz} = -\frac{8}{15}\epsilon_R\eta^4. \quad (14)$$

The soliton amplitude is not affected by delayed Raman response in $O(\epsilon_R)$ [20–22]. Therefore, the dynamics of the soliton amplitude is still given by Eqs. (4) and (5). Substituting $\eta(z)$ from Eq. (5) into Eq. (14) and integrating with respect to z , we obtain:

$$\beta(z) = \beta(0) - \frac{\epsilon_R\eta_0^2}{5\epsilon_3} \left\{ \ln \left[\frac{\eta_0^2 - \eta^2(0) + \eta^2(0) \exp(8\epsilon_3\eta_0^2 z/3)}{\eta_0^2} \right] + \frac{\eta^2(0)}{\eta_0^2} - \frac{\eta^2(0)}{\eta^2(0) + [\eta_0^2 - \eta^2(0)] \exp(-8\epsilon_3\eta_0^2 z/3)} \right\}. \quad (15)$$

The soliton position and phase are affected by the perturbations only via the dependence of η and β on z .

Numerical simulations. Equation (13) is numerically solved on a domain $[t_{\min}, t_{\max}] = [-400, 400]$ with periodic boundary conditions. The initial condition is in the form of a single NLS soliton with amplitude $\eta(0)$, frequency $\beta(0) = 0$, position $y(0) = 0$, and phase $\alpha(0) = 0$. As a typical example, we present here the results of the simulations with $\epsilon_3 = 0.01$, $\epsilon_R = 0.04$, and $\eta(0) = 0.8$. We point out that similar results are obtained for other physical parameters values. Due to the presence of delayed Raman response and the relatively large propagation distance, the soliton experiences a very large position shift. For example, for $\epsilon_R = 0.04$, $\eta(0) = 1$, and $\tilde{z} = 750$, we find using the adiabatic perturbation theory that the

soliton position shift at $\tilde{z} = 750$ is $y(\tilde{z}) = 8\epsilon_R\eta^4(0)\tilde{z}^2/15 = 12000$. Carrying out numerical simulations for transmission in an open optical waveguide setup, i.e., in a setup in which the soliton does not reach the computational domain's boundaries, is prohibitively time consuming, since one has to employ a computational domain with a size exceeding 12000. We therefore choose to work with a numerical simulations setup, in which the soliton passes through the computational domain's boundaries multiple times during the simulation. In such setup, we do *not* use damping at the boundaries, since such damping leads to the soliton's destruction. Note that the numerical simulations setup used in the current section corresponds to soliton propagation in a closed optical waveguide loop. This setup is very relevant for applications, since many long-distance transmission experiments are carried out in closed waveguide loops, see. e.g., Refs. [2, 5–10] and references therein. The values of the transmission quality distance and the final propagation distance obtained in the simulations were $z_q = 378$ and $z_f = 785$.

Figure 9 shows the pulse shape $|\psi(t, z)|$ at $z = z_q$ and at $z = z_f$, obtained in the simulations together with the prediction of the adiabatic perturbation theory, obtained with Eqs. (B1) and (5). As seen in Figs. 9(a), 9(b), and 9(c), the numerically obtained pulse shape at $z = z_q$ is close to the analytic prediction, although, a noticeable radiative tail exists at this distance. We observe that the radiative tail is highly oscillatory and is spread over the entire computational domain at $z = z_q$. The oscillatory nature of the radiative tail is attributed to the presence of delayed Raman response. The spread of radiation over the entire computational domain is due to additional emission of radiation induced by the presence of delayed Raman response, the closed waveguide loop setup, which leads to accumulation of radiation, and the smaller size of the computational time domain compared with the one used in the simulations in section II. We also observe that the radiative tail continues to grow as the soliton continues to propagate along the waveguide [see Figs. 9(d) and 9(e)]. As a result, the value of the transmission quality integral $I(z)$ increases from 0.075 at $z_q = 378$ to 0.6565 at $z_f = 785$ [see Fig. 10].

Further insight into transmission quality degradation and pulse dynamics is gained from the shape of the Fourier spectrum $|\hat{\psi}(\omega, z)|$. Figure 11 shows the numerically obtained $|\hat{\psi}(\omega, z)|$ at $z = z_q$ and at $z = z_f$ together with the prediction of the adiabatic perturbation theory, obtained with Eqs. (B3), (5), and (15). It is clear that the Fourier spectrum of the optical field for waveguides with frequency independent linear gain, cubic loss, and

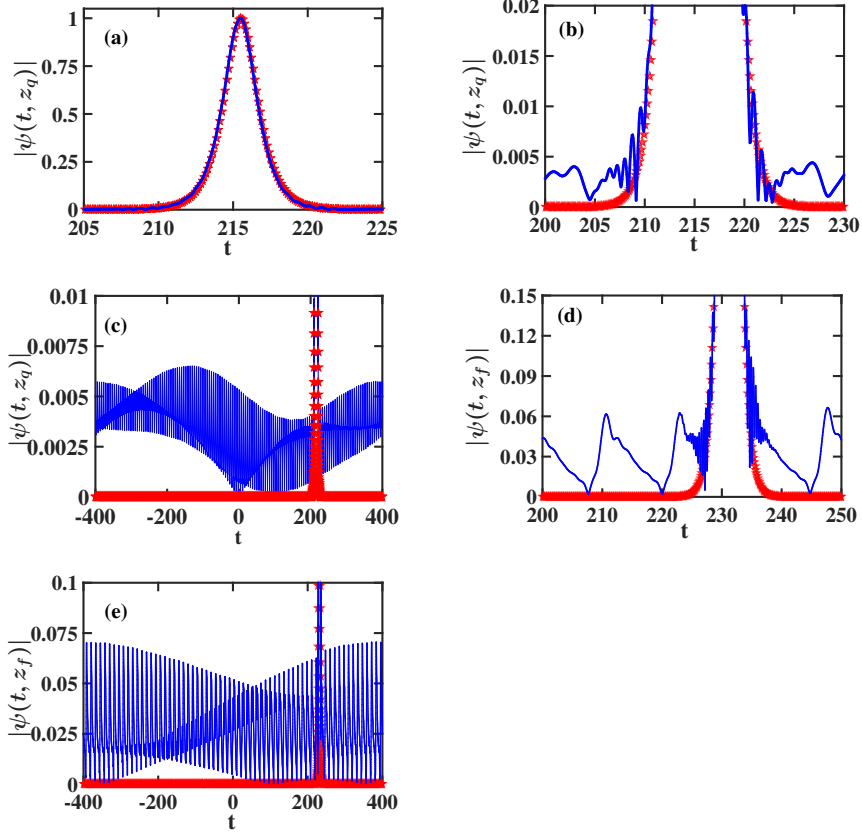


FIG. 9: The pulse shape $|\psi(t, z)|$ at $z_q = 378$ [(a), (b), and (c)] and at $z_f = 785$ [(d) and (e)] for soliton propagation in a closed optical waveguide loop with weak frequency independent linear gain, cubic loss, and delayed Raman response. The cubic loss coefficient is $\epsilon_3 = 0.01$, the Raman coefficient is $\epsilon_R = 0.04$, and the initial soliton amplitude is $\eta(0) = 0.8$. The solid blue curve corresponds to the result obtained by numerical simulations with Eq. (13), while the red stars correspond to the perturbation theory prediction of Eqs. (B1) and (5).

delayed Raman response is very different from the Fourier spectrum observed in section II for soliton propagation in the absence of delayed Raman response. More specifically, the soliton's Fourier spectrum in the current waveguide setup is centered about the nonzero z dependent soliton's frequency $\beta(z)$ and is shifted relative to the radiation's spectrum, which is centered near $\omega = 0$. The separation between the soliton's spectrum and the radiation's spectrum, which is a result of the Raman self-frequency shift experienced by the soliton, is already very clear at $z = z_q$ [see Figs. 11(a) and 11(b)]. It continues to grow with increasing z due to the increase in $|\beta(z)|$ [see Fig. 11(d)]. As a result of the separation between the two spectra, the soliton part of the numerically obtained graph of $|\hat{\psi}(\omega, z)|$ does not contain

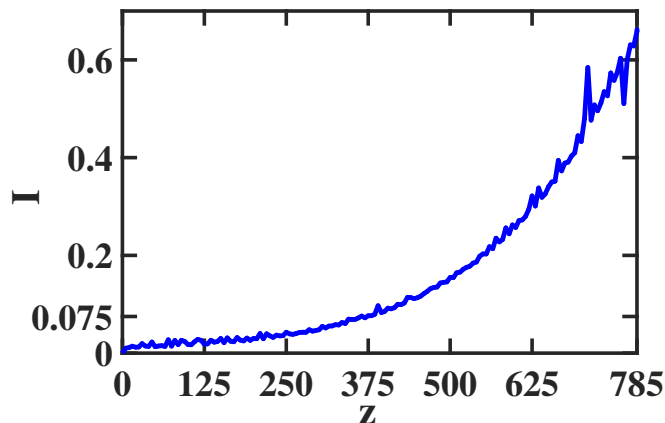


FIG. 10: The z dependence of the transmission quality integral $I(z)$ obtained by numerical simulations with Eq. (13) for the same optical waveguide setup considered in Fig. 9.

fast oscillations and is very close to the prediction of the adiabatic perturbation theory [see Fig. 11(c)]. In contrast, in the waveguides considered in section II, the Fourier spectrum of the entire optical field (soliton + radiation) is centered about $\omega = 0$. That is, there is no significant separation between the soliton and the radiation spectra. Therefore, for the waveguides considered in section II, the deviation of the numerically obtained Fourier spectrum from the spectrum expected for an NLS soliton is significant already at $z = z_q$.

The z dependence of the soliton's amplitude and frequency obtained in the simulations is shown in Figs. 12(a) and 12(b). Also shown are the adiabatic perturbation theory predictions for $\eta(z)$ and $\beta(z)$, which are given by Eqs. (5) and (15), respectively. In both graphs we observe good agreement between the numerical and analytic results for $0 \leq z \leq 500$, whereas for $500 < z \leq 785$, the difference between the two results becomes significant. Based on this comparison, we conclude that the dynamics of soliton amplitude and frequency becomes unstable for distances larger than 500. We notice that the deviation of the numerical result from the analytic result for $\eta(z)$ in the current waveguide setup is larger compared with the deviation found for soliton propagation in the absence of delayed Raman response in section II. We attribute this larger deviation to the presence of a larger radiative tail [compare Fig. 9(e) with Figs. 1(e) and 5(e)]. The radiative tail in the current waveguide setup is larger compared with the radiative tail in the waveguide setups of section II due to additional emission of radiation induced by the presence of delayed Raman response, the closed waveguide loop setup, which leads to accumulation of radiation, and the smaller size

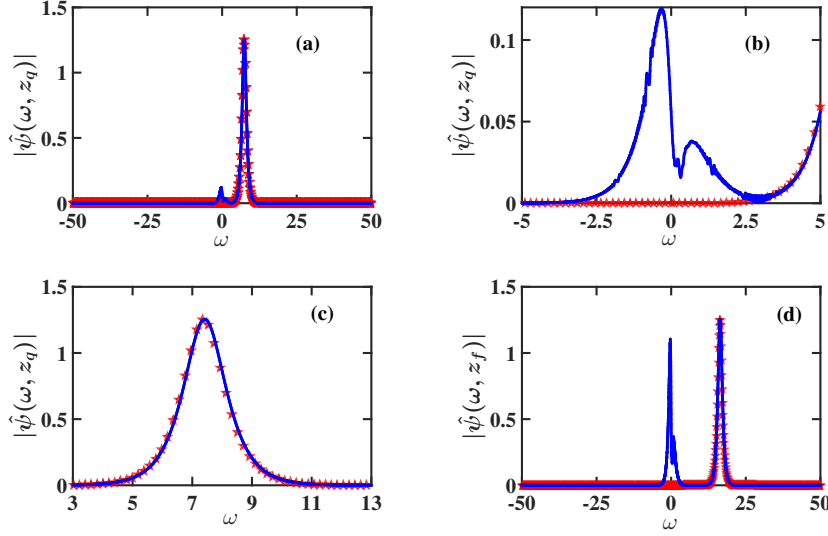


FIG. 11: The Fourier transform of the pulse shape $|\hat{\psi}(\omega, z)|$ at $z_q = 378$ [(a), (b), and (c)] and at $z_f = 785$ (d) for soliton propagation in a closed optical waveguide loop with weak frequency independent linear gain, cubic loss, and delayed Raman response. The physical parameter values are the same as in Fig. 9. The solid blue curve represents the result obtained by numerical simulations with Eq. (13) and the red stars correspond to the prediction of the adiabatic perturbation theory, obtained with Eqs. (B3), (5), and (15).

of the computational time domain used in the simulations.

B. Waveguides with frequency dependent linear gain-loss, cubic loss, and delayed Raman response

We saw in section III A that the presence of delayed Raman response in optical waveguides with frequency independent linear gain and cubic loss leads to strong separation of the soliton's Fourier spectrum from the radiation's Fourier spectrum. Thus, we expect that the replacement of the frequency independent linear gain by frequency dependent linear gain-loss of a form similar to the one in Eq. (7) will lead to efficient suppression of radiation emission and to significant enhancement of transmission quality. We therefore turn to investigate soliton propagation in nonlinear optical waveguides in the presence of weak frequency dependent linear gain-loss, cubic loss, and delayed Raman response. The propagation is

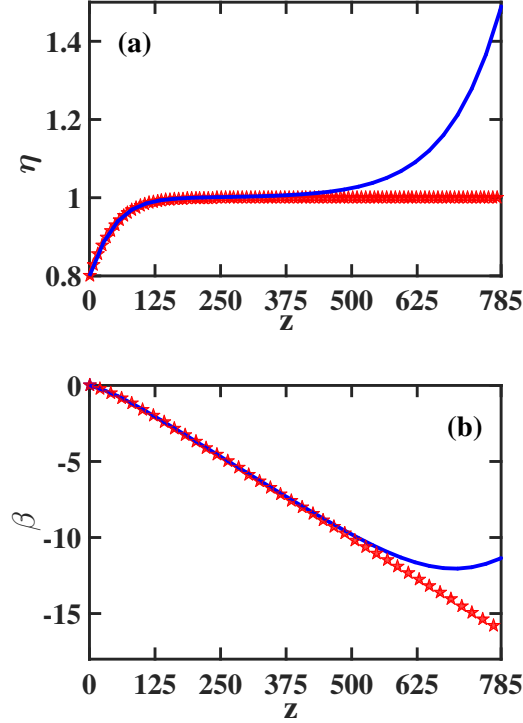


FIG. 12: The z dependence of the soliton amplitude $\eta(z)$ (a) and frequency $\beta(z)$ (b) for the closed optical waveguide loop setup considered in Figs. 9-11. The solid blue curves represent the results obtained by numerical simulations with Eq. (13). The red stars correspond to the perturbation theory predictions of Eq. (5) in (a) and of Eq. (15) in (b).

described by the following perturbed NLS equation [16, 17]:

$$i\partial_z\psi + \partial_t^2\psi + 2|\psi|^2\psi = i\mathcal{F}^{-1}(\hat{g}(\omega, z)\hat{\psi})/2 - i\epsilon_3|\psi|^2\psi + \epsilon_R\psi\partial_t|\psi|^2. \quad (16)$$

The form of the frequency and distance dependent linear gain-loss $\hat{g}(\omega, z)$ is similar to the one in Eq. (7), apart from a replacement of the initial soliton frequency $\beta(0)$ by the z dependent soliton frequency $\beta(z)$. Thus, $\hat{g}(\omega, z)$ is given by:

$$\begin{aligned} \hat{g}(\omega, z) = & -g_L + \frac{1}{2}(g_0 + g_L) [\tanh\{\rho[\omega + \beta(z) + W/2]\} \\ & - \tanh\{\rho[\omega + \beta(z) - W/2]\}]. \end{aligned} \quad (17)$$

A similar form was used in Refs. [16, 17] in studies of multisequence soliton-based transmission in the presence of delayed Raman response and different transmission stabilizing mechanisms based on frequency dependent gain-loss. In the limit $\rho \gg 1$, $\hat{g}(\omega, z)$ can be

approximated by the following step function:

$$\hat{g}(\omega, z) \simeq \begin{cases} g_0 & \text{if } -\beta(z) - W/2 < \omega \leq -\beta(z) + W/2, \\ -g_L & \text{elsewhere.} \end{cases} \quad (18)$$

We observe that the weak linear gain g_0 in the frequency interval $(-\beta(z) - W/2, -\beta(z) + W/2]$ balances the effects of cubic loss, such that the soliton amplitude approaches the equilibrium value η_0 with increasing z . Additionally, the relatively strong linear loss g_L leads to suppression of emission of radiation with frequencies outside of the interval $(-\beta(z) - W/2, -\beta(z) + W/2]$. Thus, due to the relatively large separation between the soliton's spectrum and the radiation's spectrum expected for the current waveguide setup, the introduction of the frequency dependent linear gain-loss $\hat{g}(\omega, z)$ of Eq. (17) is expected to lead to efficient suppression of radiation emission and to significant enhancement of transmission quality.

Since the soliton amplitude is not affected by delayed Raman response in $O(\epsilon_R)$, the dynamics of the amplitude is still described by Eq. (11). In addition, the dynamics of the soliton frequency is given by Eq. (14). The soliton position and phase are affected by the perturbations only via the dependence of η and β on z .

Numerical simulations. To check whether the interplay between frequency dependent linear gain-loss and delayed Raman response leads to enhanced transmission quality, we perform numerical simulations with Eqs. (16) and (17). The equations are numerically integrated on a domain $[t_{\min}, t_{\max}] = [-400, 400]$ with periodic boundary conditions. The initial condition is in the form of a single NLS soliton with amplitude $\eta(0)$, frequency $\beta(0) = 0$, position $y(0) = 0$, and phase $\alpha(0) = 0$. To enable comparison with the results of the numerical simulations in sections II and III A, we use the same parameter values that were used in those sections. That is, we carry out the simulations with $\epsilon_3 = 0.01$, $\epsilon_R = 0.04$, $\eta(0) = 0.8$, $W = 10$, $\rho = 10$, and $g_L = 0.5$. We emphasize, however, that similar results are obtained for other physical parameters values. Similar to the simulations in section III A, the soliton passes multiple times through the computational domain's boundaries during the simulation, i.e., the simulation describes soliton propagation in a closed waveguide loop. To avoid soliton destruction, we do not employ damping at the boundaries. The simulation is run up to a pre-determined final propagation distance $z_f = 2000$, at which the value of the transmission quality integral is still smaller than 0.075.

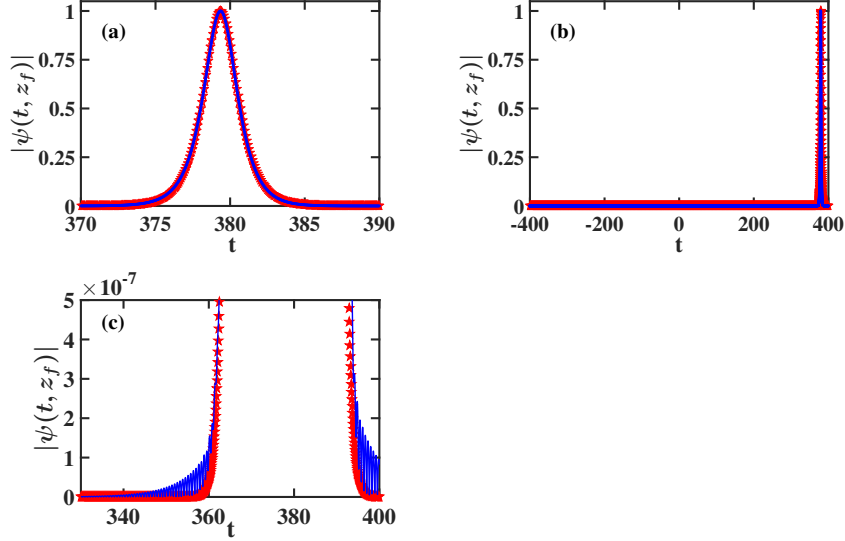


FIG. 13: The pulse shape $|\psi(t, z_f)|$, where $z_f = 2000$, for soliton propagation in a closed optical waveguide loop with weak frequency dependent linear gain-loss, cubic loss, and delayed Raman response. The cubic loss coefficient is $\epsilon_3 = 0.01$, the Raman coefficient is $\epsilon_R = 0.04$, the initial soliton amplitude is $\eta(0) = 0.8$, and the parameters of the linear gain-loss $\hat{g}(\omega, z)$ in Eq. (17) are $W = 10$, $\rho = 10$, and $g_L = 0.5$. The solid blue curve corresponds to the result obtained by numerical simulations with Eqs. (16) and (17). The red stars correspond to the prediction of the adiabatic perturbation theory, obtained with Eqs. (B1) and (11).

Figure 13 shows the pulse shape $|\psi(t, z)|$ at $z = z_f$, as obtained in the simulations. The prediction of the adiabatic perturbation theory, obtained with Eqs. (B1) and (11), is also shown. As seen in Figs. 13(a) and 13(b), the numerically obtained pulse shape at $z = z_f$ is very close to the analytic prediction and no significant radiative tail is observed. Moreover, as seen in Fig. 13(c), the deviation of the numerical result for $|\psi(t, z_f)|$ from the theoretical one is smaller than 10^{-6} for all t values. Thus, the interplay between frequency dependent linear gain-loss and delayed Raman response does lead to significant enhancement of transmission quality compared with the waveguide setups considered in sections II and III A. The enhancement of transmission quality is also demonstrated in Fig. 14, which shows the numerically obtained $I(z)$ curve and the average $\langle I(z) \rangle$, which is defined by $\langle I(z) \rangle \equiv \int_0^{z_f} dz' I(z') / z_f$. As seen in this figure, the value of $I(z)$ remains smaller than 0.032 throughout the propagation and $\langle I(z) \rangle = 0.0156$.

The enhanced transmission quality can be explained with the help of the Fourier trans-

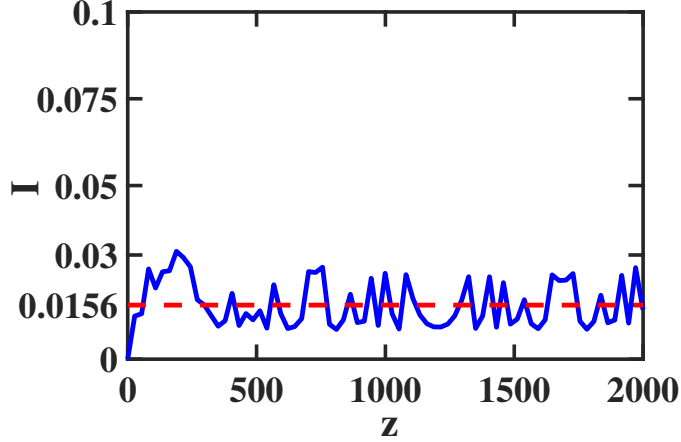


FIG. 14: The z dependence of the transmission quality integral $I(z)$ obtained by numerical simulations with Eqs. (16) and (17) for the same optical waveguide setup considered in Fig. 13. The solid blue curve represents $I(z)$ and the dashed red horizontal line corresponds to $\langle I(z) \rangle$.

form of the pulse $|\hat{\psi}(\omega, z)|$. Figure 15 shows the numerically obtained Fourier transform $|\hat{\psi}(\omega, z)|$ at $z = z_f$ together with the prediction of the adiabatic perturbation theory, obtained with Eqs. (B3), (11), and (14). We observe very good agreement between the two results. More specifically, in both curves, the Fourier spectrum of the soliton is strongly downshifted and is centered about the frequency $\omega_m = -\beta(z_f) = 42.0$. Additionally, the numerically obtained curve of $|\hat{\psi}(\omega, z_f)|$ does not contain any fast oscillations in the main peak such as the oscillations seen in Figs. 3 and 7 (in section II) for soliton propagation in the absence of delayed Raman response. Furthermore, the numerically obtained curve of $|\hat{\psi}(\omega, z_f)|$ does not contain any significant “radiation peaks” such as the one seen in Fig. 11 (in section III A) for waveguides with frequency independent linear gain, cubic loss, and delayed Raman response. Based on these observations we conclude that the presence of delayed Raman response leads to separation of the soliton’s spectrum from the radiation’s spectrum via the soliton self-frequency shift, while the frequency dependent linear gain-loss leads to efficient suppression of radiation emission. As a result, transmission quality is significantly enhanced in waveguides with frequency dependent linear gain-loss, cubic loss, and delayed Raman response compared with the waveguide setups considered in sections II and III A.

The enhancement of transmission quality in waveguides with frequency dependent linear gain-loss, cubic loss, and delayed Raman response is also manifested in the dynamics of

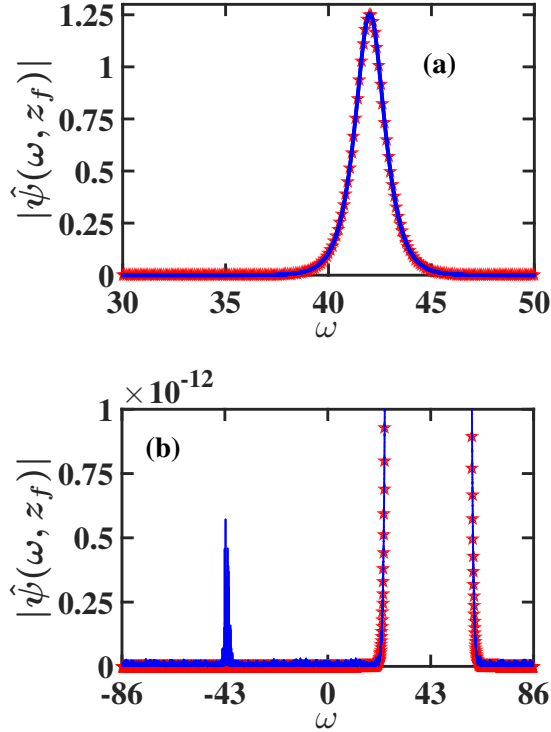


FIG. 15: The Fourier transform of the pulse shape $|\hat{\psi}(\omega, z)|$ at $z_f = 2000$ for soliton propagation in a closed optical waveguide loop with weak frequency dependent linear gain-loss, cubic loss, and delayed Raman response. The physical parameter values are the same as in Fig. 13. The solid blue curve represents the result obtained by numerical simulations with Eqs. (16) and (17). The red stars correspond to the prediction of the adiabatic perturbation theory, obtained with Eqs. (B3), (11), and (14).

the soliton's amplitude and frequency. Figures 16(a) and 16(b) show the z dependence of the soliton's amplitude and frequency obtained in the simulations. Also shown are the predictions of the adiabatic perturbation theory, obtained with Eqs. (11) and (14). We observe that the numerically obtained soliton amplitude tends to the equilibrium value $\eta_0 = 1$ at short distances and stays close to this value throughout the propagation, in excellent agreement with the perturbation theory prediction. Furthermore, the value of the soliton frequency obtained in the simulations remains close to the z dependent value predicted by the adiabatic perturbation theory throughout the propagation. Thus, the efficient suppression of radiation emission in waveguides with frequency dependent linear gain-loss, cubic loss, and delayed Raman response enables observation of stable amplitude

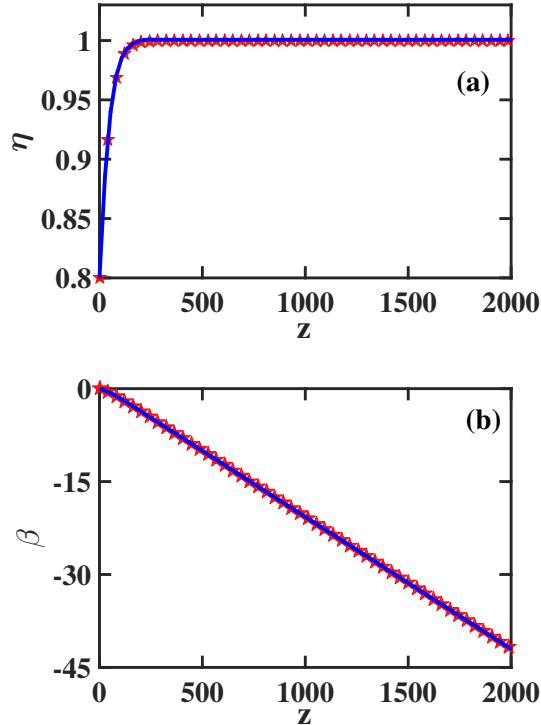


FIG. 16: The z dependence of the soliton amplitude $\eta(z)$ (a) and frequency $\beta(z)$ (b) for the closed optical waveguide loop setup considered in Figs. 13-15. The solid blue curves represent the results obtained by numerical simulations with Eqs. (16) and (17). The red stars correspond to the predictions of the adiabatic perturbation theory, obtained with Eq. (11) in (a) and with Eqs. (14) and (11) in (b).

and frequency dynamics along significantly larger distances compared with the distances obtained with the closed optical waveguide loop setup considered in section III A. We also point out that the waveguide setups considered in the current subsection can be used for inducing large frequency shifts, which are not accompanied by pulse distortion, in soliton-based optical waveguide transmission systems.

IV. PULSE DYNAMICS IN WAVEGUIDES WITH LINEAR GAIN, CUBIC LOSS, AND GUIDING FILTERS

Introduction. The enhancement of transmission quality and stability in waveguides with frequency dependent linear gain-loss and delayed Raman response, which was demonstrated in subsection III B, is somewhat similar to transmission stability enhancement in waveguides

with linear gain and guiding filters with a varying central frequency. Indeed, in the latter waveguides, the guiding filters play a role similar to that of the frequency dependent linear gain-loss, i.e., their presence leads to suppression of radiation emission with frequencies that are significantly different from the soliton's frequency. In addition, the variation of the central frequency of the guiding filters with propagation distance plays a role similar to that of the Raman self-frequency shift, that is, it leads to the separation of the soliton's Fourier spectrum from the radiation's Fourier spectrum. For this reason it is useful to compare the dynamics of optical solitons in the two waveguide systems. We therefore turn to study soliton propagation in optical waveguide loops with frequency independent linear gain, cubic loss, and optical guiding filters. We start by considering guiding filters with a constant central frequency in subsection IV A, and treat the case of guiding filters with a varying central frequency in subsection IV B. We point out that stabilization of soliton-based transmission in optical fibers by guiding filters with a varying central frequency was theoretically and experimentally demonstrated in Refs. [2, 5, 6, 9, 64]. Since these studies focused on optical fiber transmission, the effects of cubic loss were neglected. In the current section, we extend the theoretical treatment of Refs. [2, 5, 64] and take into account the effects of cubic loss in addition to the effects of linear gain and guiding filters.

A. Waveguides with linear gain, cubic loss, and guiding filters with a constant central frequency

We consider propagation of pulses of light in nonlinear optical waveguides in the presence of weak linear gain, weak cubic loss, and guiding optical filters. Following the treatment in Refs. [2, 5, 64], we assume that the response function of the optical filter can be approximated by a Gaussian with a maximum that is equal to 1 and that is located at the frequency ω_p . Under this assumption, the propagation is described by the following perturbed NLS equation [2, 5, 64]:

$$i\partial_z\psi + \partial_t^2\psi + 2|\psi|^2\psi = ig_0\psi/2 - i\epsilon_3|\psi|^2\psi - i\epsilon_\omega(i\partial_t - \omega_p)^2\psi, \quad (19)$$

where $\epsilon_\omega > 0$ is the second-order filtering coefficient, and ω_p is assumed to be constant in the current subsection [65]. Equation (19) can also be written as

$$i\partial_z\psi + \partial_t^2\psi + 2|\psi|^2\psi = i(g_0/2 - \epsilon_\omega\omega_p^2)\psi - i\epsilon_3|\psi|^2\psi - 2\epsilon_\omega\omega_p\partial_t\psi + i\epsilon_\omega\partial_t^2\psi. \quad (20)$$

Using the adiabatic perturbation theory for the NLS soliton, we find that the dynamics of the soliton's amplitude and frequency is given by:

$$\frac{d\eta}{dz} = \eta \{g_0 - 2\epsilon_\omega [\eta^2/3 + (\beta - \omega_p)^2] - 4\epsilon_3\eta^2/3\}, \quad (21)$$

and

$$\frac{d\beta}{dz} = -4\epsilon_\omega (\beta - \omega_p) \eta^2/3. \quad (22)$$

In the current subsection, we try to realize stable transmission with constant amplitude $\eta = \eta_0 > 0$ and frequency $\beta = \beta_0$. We therefore require that (η_0, β_0) is an equilibrium point of Eqs. (21) and (22). We obtain: $g_0 = 2\epsilon_\omega\eta_0^2/3 + 4\epsilon_3\eta_0^2/3$ and $\beta_0 = \omega_p$. As a result, Eq. (21) takes the form

$$\frac{d\eta}{dz} = 2\eta [2\epsilon_3 (\eta_0^2 - \eta^2)/3 + \epsilon_\omega (\eta_0^2 - \eta^2)/3 - \epsilon_\omega (\beta - \omega_p)^2]. \quad (23)$$

Thus, dynamics of the soliton's amplitude and frequency is described by Eqs. (22) and (23). Linear stability analysis shows that (η_0, ω_p) is a stable node of the system (22)-(23). In addition to the equilibrium point at (η_0, ω_p) there is a line of equilibrium points at $(0, \beta)$. These additional equilibrium points are asymptotically stable for $\beta > \omega_p + r_p\eta_0$ or $\beta < \omega_p - r_p\eta_0$ and are unstable for $\omega_p - r_p\eta_0 < \beta < \omega_p + r_p\eta_0$, where $r_p = [(2\epsilon_3 + \epsilon_\omega)/(3\epsilon_\omega)]^{1/2}$. Note that similar stability conditions hold for small amplitude wave solutions of the form $\psi_l(t, z) = \bar{C} \exp(-ikz + i\omega t)$ of the propagation model

$$i\partial_z\psi + \partial_t^2\psi = ig_0\psi/2 - i\epsilon_\omega (i\partial_t - \omega_p)^2\psi, \quad (24)$$

which is the linear part of Eq. (19). Indeed, substitution of $\psi_l(t, z)$ into Eq. (24) yields

$$k(\omega) = \omega^2 + i [g_0/2 - \epsilon_\omega(\omega + \omega_p)^2]. \quad (25)$$

As a result, the small amplitude wave solutions $\psi_l(t, z)$ are stable for

$$\omega < -\omega_p - r_p\eta_0 \quad \text{or} \quad \omega > -\omega_p + r_p\eta_0, \quad (26)$$

and are unstable for

$$-\omega_p - r_p\eta_0 < \omega < -\omega_p + r_p\eta_0. \quad (27)$$

Furthermore, Eq. (25) also indicates that suppression of radiation emission by the guiding filters is more efficient at frequencies that are far from the equilibrium value of the soliton's frequency ω_p (see also Refs. [2, 5, 64]).

Numerical simulations. Equation (20) is numerically solved on a domain $[t_{\min}, t_{\max}] = [-400, 400]$ with periodic boundary conditions. The initial condition is in the form of a single NLS soliton with amplitude $\eta(0)$, frequency $\beta(0)$, position $y(0) = 0$, and phase $\alpha(0) = 0$. As a typical example, we present here the results of the simulations with $\epsilon_3 = 0.01$, $\epsilon_\omega = 0.04$, $\omega_p = 42.7$, $\eta(0) = 0.8$, and $\beta(0) = 42.5$. This choice of the physical parameter values enables comparison with results of numerical simulations in previous sections and in section IV B. We point out that similar results are obtained for other physical parameters values. Due to the presence of the guiding filters and due to the initial nonzero soliton frequency, the soliton experiences a very large position shift during the propagation. As a result, the soliton passes through the computational domain's boundaries multiple times during the simulation. To avoid soliton destruction, we do not employ damping at the boundaries. Thus, the simulations describe soliton propagation in a closed optical waveguide loop. The values of the transmission quality distance and the final propagation distance obtained in the simulations are $z_q = 96$ and $z_f = 208$.

Figure 17 shows the pulse shape $|\psi(t, z)|$ at $z = z_q$ and at $z = z_f$, obtained in the simulations. Also shown is a comparison with the prediction of the adiabatic perturbation theory, obtained with Eqs. (B1), (22), and (23). As seen in Figs. 17(a) and 17(b), the pulse shape obtained in the simulations at $z = z_q$ is close to the analytic prediction. However, the comparison of the analytic prediction with the numerical result for small $|\psi(t, z_q)|$ values in Fig. 17(c) shows that an appreciable radiative tail exists at $z = z_q$. Additionally, as seen in Figs. 17(d) and 17(e), the radiative tail continues to grow as the soliton continues to propagate along the waveguide. As a result, the value of the transmission quality integral $I(z)$ increases from 0.075 at $z_q = 96$ to 0.6674 at $z_f = 208$ [see Fig. 18]. We note that the radiative tail observed for the current optical waveguide setup is much larger than the

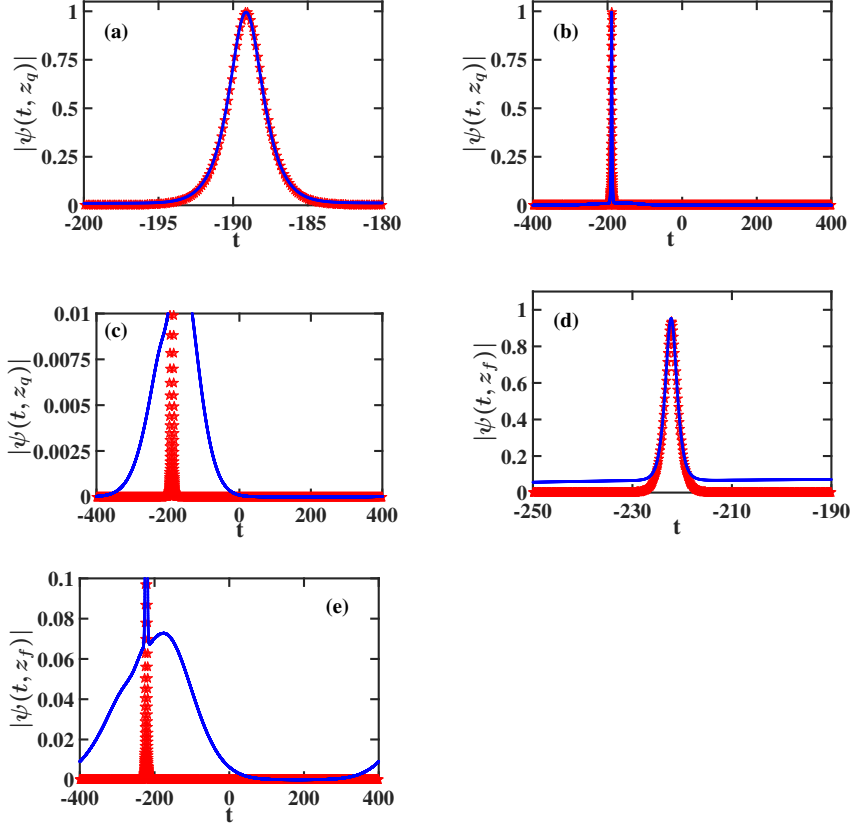


FIG. 17: The pulse shape $|\psi(t, z)|$ at $z_q = 96$ [(a), (b), and (c)] and at $z_f = 208$ [(d) and (e)] for soliton propagation in a closed optical waveguide loop with weak frequency independent linear gain, cubic loss, and guiding filters with a constant central frequency. The physical parameter values are $\epsilon_3 = 0.01$, $\epsilon_\omega = 0.04$, $\omega_p = 42.7$, $\eta(0) = 0.8$, and $\beta(0) = 42.5$. The solid blue curve represents the result obtained by numerical simulations with Eq. (20), while the red stars correspond to the perturbation theory prediction of Eqs. (B1), (22), and (23).

radiative tail observed in section II for waveguides with linear gain or loss and cubic loss and with no guiding filters [compare Fig. 17(c) with Figs. 1(c) and 5(c)]. In addition, the z_q and z_f values for the current waveguide setup are considerably smaller compared with the z_q and z_f values obtained with the waveguide setups of section II. Based on these findings we deduce that transmission quality in waveguide loops with weak frequency independent linear gain, cubic loss, and guiding filters with a constant central frequency is significantly reduced compared with the waveguide setups considered in section II.

The reduction in transmission quality of the waveguides considered in the current subsection compared with the waveguides considered in section II can be partially attributed to

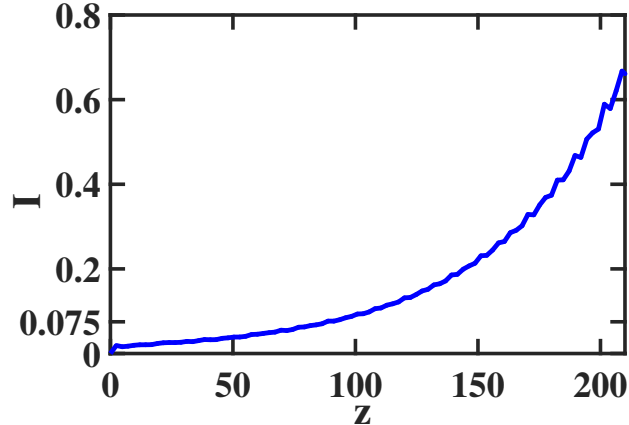


FIG. 18: The z dependence of the transmission quality integral $I(z)$ obtained by numerical simulations with Eq. (20) for the same optical waveguide setup considered in Fig. 17.

the following factors. First, the closed waveguide loop setup, which leads to accumulation of radiation, and second, the smaller size of the computational domain used in the simulations in the current subsection. The other major factors leading to the reduced transmission quality can be explained by analyzing the dynamics of the Fourier transform of the optical field $|\hat{\psi}(\omega, z)|$. Figure 19 shows the numerically obtained $|\hat{\psi}(\omega, z)|$ at $z = z_q$ and at $z = z_f$ together with the prediction of the adiabatic perturbation theory, obtained with Eqs. (B3), (22), and (23). We observe that the graphs of $|\hat{\psi}(\omega, z_q)|$ and $|\hat{\psi}(\omega, z_f)|$ vs ω are somewhat similar to the graphs obtained in section II for soliton propagation in waveguides with linear gain or loss and cubic loss [compare Fig. 19 with Figs. 3 and 7]. More specifically, the deviation of the numerical result from the prediction of the perturbation theory is noticeable already at $z = z_q$ and is of order 1 at $z = z_f$. This deviation appears as fast oscillations in the graph of the numerically obtained $|\hat{\psi}(\omega, z)|$ vs ω , which are most pronounced near the soliton's central frequency $\beta(z)$. Additionally, as seen in Figs. 19(b) and 19(c), the frequency interval in which the oscillations are most pronounced coincides with the instability interval in Eq. (27) for small amplitude wave solutions $\psi_l(t, z)$ of the linear propagation model (24) (for the parameter values used in the simulations, the instability interval of Eq. (27) is $-43.407 < \omega < -41.993$). Furthermore, there is no significant separation between the soliton's spectrum and the radiation's spectrum. Based on these observations we identify three additional factors besides the closed waveguide loop setup and the size of the computational domain that lead to reduced transmission quality in the current waveguide

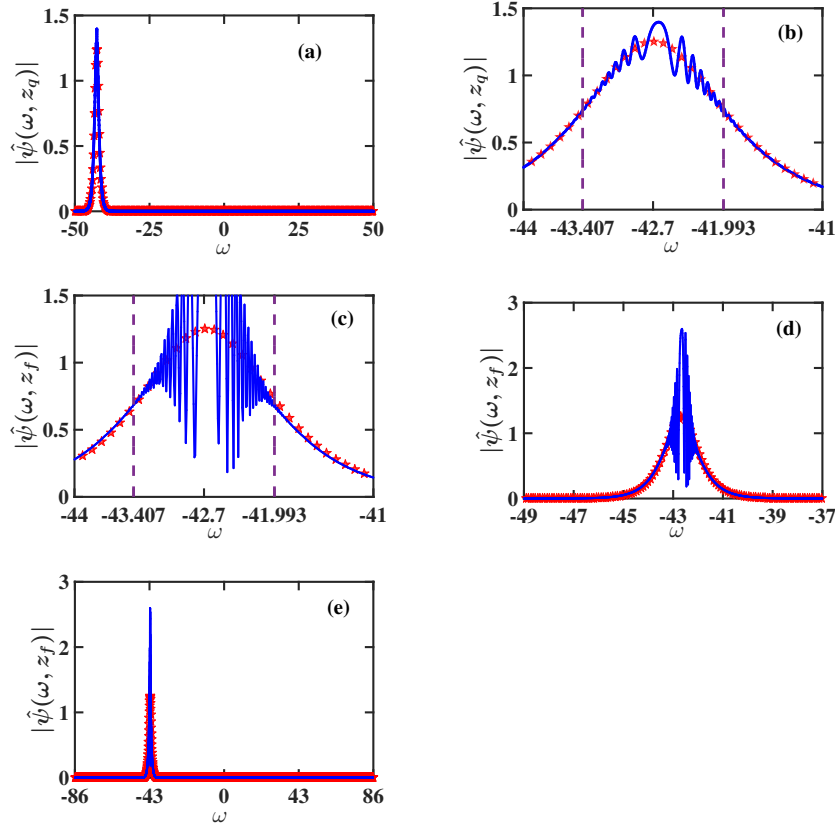


FIG. 19: The Fourier transform of the pulse shape $|\hat{\psi}(\omega, z)|$ at $z_q = 96$ [(a) and (b)] and at $z_f = 208$ [(c), (d), and (e)] for the same optical waveguide setup considered in Fig. 17. The solid blue curve represents the result obtained by numerical simulations with Eq. (20). The red stars correspond to the prediction of the adiabatic perturbation theory, obtained with Eqs. (B3), (22), and (23). The dashed purple vertical lines in (b) and (c) correspond to the end points of the instability interval of Eq. (27) for small amplitude wave solutions of Eq. (24).

setup. (1) Additional emission of radiation due to the presence of the guiding filters. (2) Instability of small amplitude waves with frequencies close to the equilibrium value of the soliton's frequency ω_p . (3) The lack of significant separation between the soliton's spectrum and the radiation's spectrum, which makes suppression of radiation emission by the guiding filters inefficient (see Eq. (25) and Refs. [2, 5, 64]). The combination of the factors (1)-(3) together with the closed waveguide loop setup and the smaller size of the computational domain leads to smaller z_q and z_f values in the current waveguide setup compared with the values obtained in section II for soliton propagation in the absence of guiding filters.

The reduction in transmission quality in waveguides with guiding filters with a constant central frequency is also manifested in the dynamics of the soliton's amplitude and frequency. Figures 20(a) and 20(b) show the z dependence of the soliton's amplitude and frequency obtained in the simulations. The predictions of the adiabatic perturbation theory, obtained with Eqs. (22) and (23), are also shown. We observe that for $0 \leq z \leq 100$, the numerically obtained amplitude and frequency tend to the equilibrium values $\eta_0 = 1$ and $\omega_p = 42.7$, in good agreement with the prediction of the adiabatic perturbation theory. However, for $100 < z \leq 208$, the numerically obtained curves of $\eta(z)$ and $\beta(z)$ deviate significantly from the curves predicted by the perturbation theory. These deviations coincide with the increase in the value of $I(z)$ observed in Fig. 18 and with the deterioration of the pulse shape observed in Figs. 17 and 19. Based on these observations and on the smaller values of z_q and z_f for the current waveguide setup compared with the values obtained for the waveguide setups considered in sections II and III, we conclude that the introduction of guiding filters with a *constant* central frequency does not lead to improvement of transmission quality.

B. Waveguides with linear gain, cubic loss, and guiding filters with a varying central frequency

As we saw in subsection IV A, suppression of radiation emission in waveguides with guiding filters with a constant central frequency is inefficient due to the lack of significant separation between the soliton's spectrum and the radiation's spectrum. This leads to reduced transmission quality for these waveguides. However, as shown in Refs. [2, 5, 64] (for optical fibers), this drawback can be circumvented by using guiding filters with a varying central frequency $\omega_p(z)$, which is a monotonous function of z . In this case at large distances, the soliton's spectrum is centered around a z dependent frequency $\tilde{\beta}_0 + \omega_p(z)$, while the radiation's spectrum is centered near the constant frequency $\tilde{\beta}_0$. Since $\omega_p(z)$ is a monotonous function of z , at sufficiently large z $|\omega_p(z)| \gg 1$, and therefore the radiation's spectrum is well-separated from the soliton's spectrum. As a result, in this case suppression of radiation emission by the guiding filters becomes very efficient at intermediate and large distances.

We therefore turn to study soliton propagation in the presence of weak linear gain, weak cubic loss, and guiding filters with a varying central frequency. Similar to the treatment in Refs. [2, 5, 64], we assume that the response function of the guiding filters can be

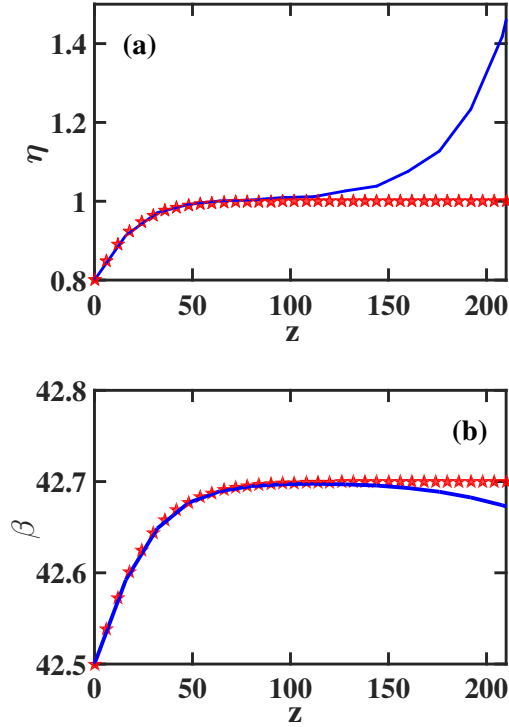


FIG. 20: The z dependence of the soliton amplitude $\eta(z)$ (a) and frequency $\beta(z)$ (b) for the closed optical waveguide loop setup considered in Figs. 17-19. The solid blue curves represent the results obtained by numerical simulations with Eq. (20). The red stars correspond to the predictions of the adiabatic perturbation theory, obtained with Eqs. (22) and (23).

approximated by a Gaussian with a maximum that is equal to 1 and that is located at the frequency $\omega_p(z)$. Thus, the propagation is described by Eq. (19) or by Eq. (20), where ω_p is now z dependent. In addition, the dynamics of the soliton's amplitude and frequency is described by Eqs. (21) and (22) in first-order in ϵ_ω and ϵ_3 . Similar to the treatment in Refs. [2, 5, 64], we assume that ω_p changes linearly with z , that is, $\omega_p = \omega'_p z$, where $\omega'_p \equiv d\omega_p/dz = C_1$, and C_1 is a constant. We define a new frequency $\tilde{\beta}$ by: $\tilde{\beta}(z) = \beta(z) - \omega_p(z)$. The new system of equations for the dynamics of η and $\tilde{\beta}$ is:

$$\frac{d\eta}{dz} = \eta \left[g_0 - 2\epsilon_\omega \left(\eta^2/3 + \tilde{\beta}^2 \right) - 4\epsilon_3 \eta^2/3 \right], \quad (28)$$

and

$$\frac{d\tilde{\beta}}{dz} = -C_1 - 4\epsilon_\omega \tilde{\beta} \eta^2/3. \quad (29)$$

We are interested in realizing stable transmission with constant amplitude $\eta = \eta_0 > 0$ and frequency $\tilde{\beta} = \tilde{\beta}_0 \neq 0$. We therefore require that $(\eta_0, \tilde{\beta}_0)$ is an equilibrium point of Eqs. (28) and (29). We obtain: $g_0 = 2\epsilon_\omega \eta_0^2/3 + 2\epsilon_\omega \tilde{\beta}_0^2 + 4\epsilon_3 \eta_0^2/3$ and $\tilde{\beta}_0 = -3\omega'_p/(4\epsilon_\omega \eta_0^2)$. Thus, Eq. (28) takes the form

$$\frac{d\eta}{dz} = 2\eta \left[2\epsilon_3 (\eta_0^2 - \eta^2)/3 + \epsilon_\omega (\eta_0^2 - \eta^2)/3 + \epsilon_\omega (\tilde{\beta}_0^2 - \tilde{\beta}^2) \right]. \quad (30)$$

Dynamics of the soliton's amplitude and frequency is therefore described by Eqs. (29) and (30). Linear stability analysis shows that $(\eta_0, \tilde{\beta}_0)$ is a stable equilibrium point of the system (29)-(30) [a stable node], provided that ω'_p satisfies the condition

$$|\omega'_p| < \left(\frac{8}{27} \right)^{1/2} \epsilon_\omega \left(1 + \frac{2\epsilon_3}{\epsilon_\omega} \right)^{1/2} \eta_0^3. \quad (31)$$

Numerical simulations. Equation (20) is numerically integrated on a domain $[t_{\min}, t_{\max}] = [-400, 400]$ with periodic boundary conditions. The initial condition is in the form of an NLS soliton with amplitude $\eta(0)$, frequency $\beta(0) = 0$, position $y(0) = 0$, and phase $\alpha(0) = 0$. To enable comparison with the results of the numerical simulations in subsection IV A, we use parameter values that are similar to the ones used in this subsection. In particular, we carry out the simulations with $\epsilon_3 = 0.01$, $\epsilon_\omega = 0.04$, $\omega_p(0) = 0$, and $\eta(0) = 0.8$. We realize efficient separation between the soliton's spectrum and the radiation's spectrum by choosing $\omega'_p = 0.0218$, which is close to the largest value allowed by inequality (31). We emphasize, however, that similar results are obtained for other values of the physical parameters. Similar to the simulations in sections III and IV A, the soliton passes multiple times through the computational domain's boundaries during the simulation and therefore the simulation describes soliton propagation in a closed waveguide loop. To avoid soliton destruction, we do not employ damping at the boundaries. The simulation is run up to a final propagation distance $z_f = 2000$, at which the value of the transmission quality integral $I(z)$ is still smaller than 0.075.

Figure 21 shows the pulse shape $|\psi(t, z)|$ at $z = z_f$, as obtained in the simulations. Also shown is the prediction of the adiabatic perturbation theory, obtained with Eqs. (B1), (29), and (30). As seen in Figs. 21(a) and 21(b), the numerically obtained pulse shape at $z = z_f$ is very close to the analytic prediction and no significant radiative tail is observed. Furthermore, as seen in Fig. 21(c), the deviation of the numerical result for $|\psi(t, z_f)|$ from the theoretical one is smaller than 10^{-9} for all t values. Therefore, the introduction of

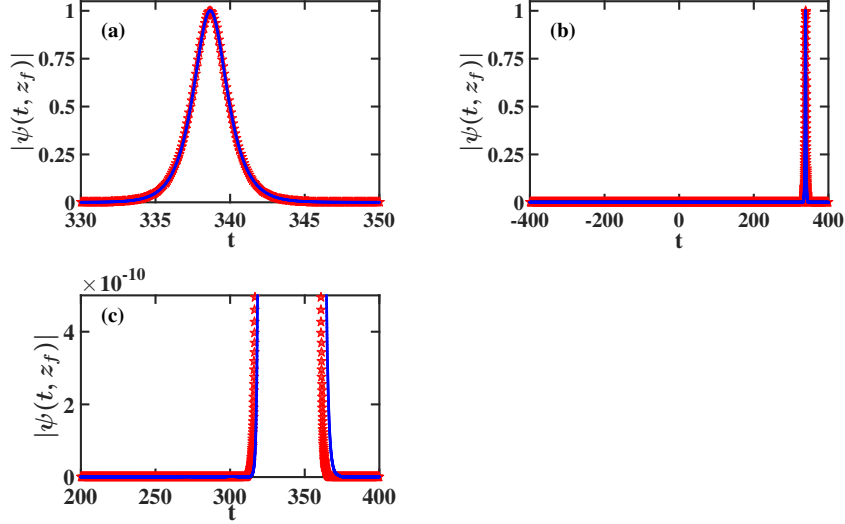


FIG. 21: The pulse shape $|\psi(t, z_f)|$, where $z_f = 2000$, for soliton propagation in a closed optical waveguide loop with weak frequency independent linear gain, cubic loss, and guiding filters with a varying central frequency. The physical parameter values are $\epsilon_3 = 0.01$, $\epsilon_\omega = 0.04$, $\omega_p(0) = 0$, $\omega'_p = 0.0218$, $\eta(0) = 0.8$, and $\beta(0) = 0$. The solid blue curve represents the result obtained by numerical simulations with Eq. (20), while the red stars correspond to the prediction of the perturbation theory, obtained with Eqs. (B1), (29), and (30).

guiding filters with a central frequency that changes linearly with propagation distance leads to significant enhancement of transmission quality compared with the waveguide setups considered in sections II, III A, and IV A. The enhancement of transmission quality is also demonstrated in Fig. 22, which shows the z dependence of the transmission quality integral I obtained in the simulations along with the average $\langle I(z) \rangle$. As seen in this figure, the value of $I(z)$ is smaller than 0.05 throughout the propagation and is smaller than 0.02 for $96 \leq z \leq 2000$. In addition, $\langle I(z) \rangle = 0.00887$

Further insight into the enhanced transmission quality can be gained from the Fourier transform of the pulse $|\hat{\psi}(\omega, z)|$. Figure 23 shows the numerically obtained Fourier transform $|\hat{\psi}(\omega, z)|$ at $z = z_f$ together with the prediction of the adiabatic perturbation theory, obtained with Eqs. (B3), (29), and (30). The agreement between the two results is excellent. In particular, the Fourier transform $|\hat{\psi}(\omega, z_f)|$ obtained in the simulation does not contain any fast oscillations in the main peak such as the oscillations seen in Figs. 3 and 7 in section II, and in Fig. 19 in section IV A. Additionally, $|\hat{\psi}(\omega, z_f)|$ does not contain any peaks

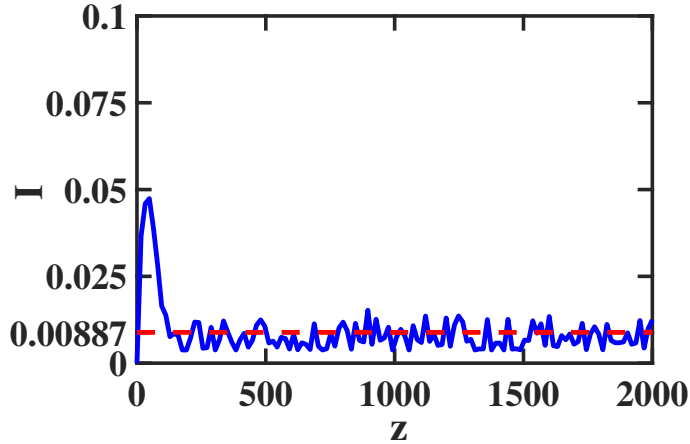


FIG. 22: The z dependence of the transmission quality integral $I(z)$ obtained by numerical simulations with Eq. (20) for the same optical waveguide setup considered in Fig. 21. The solid blue curve represents $I(z)$ and the dashed red horizontal line corresponds to $\langle I(z) \rangle$.

associated with radiation emission such as the one seen in Fig. 11 in section III A. Based on these findings and based on the comparison with the results obtained in section IV A, we deduce that the introduction of a varying central frequency of the guiding filters leads to significant enhancement of transmission quality. Similar to the situation in waveguides with delayed Raman response, the monotonous increase of the central filtering frequency ω_p leads to separation of the soliton's spectrum from the radiation's spectrum. The separation of the two spectra enables efficient suppression of radiation emission with frequencies that are significantly different from the soliton's frequency due to the presence of the guiding filters.

Figures 24(a) and 24(b) show the z dependence of the soliton's amplitude and frequency obtained in numerical simulations with Eq. (20). Also shown are the predictions of the adiabatic perturbation theory, obtained with Eqs. (29) and (30). It is seen that the numerically obtained soliton amplitude tends to the equilibrium value $\eta_0 = 1$ at short distances and stays close to this value throughout the propagation, in excellent agreement with the perturbation theory prediction. Additionally, the value of the soliton frequency obtained in the simulations remains close to the z dependent value predicted by the adiabatic perturbation theory throughout the propagation. Based on these findings and on similar results obtained for other values of the physical parameters we conclude that the efficient suppression of radiation emission in waveguides with frequency independent linear gain, cubic loss, and guiding filters with a varying central frequency enables observation of stable amplitude

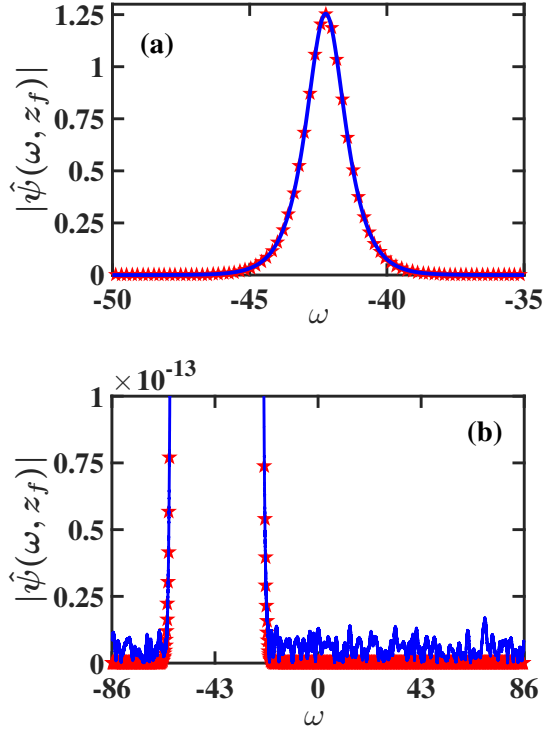


FIG. 23: The Fourier transform of the pulse shape $|\hat{\psi}(\omega, z)|$ at $z_f = 2000$ for soliton propagation in a closed optical waveguide loop with weak frequency independent linear gain, cubic loss, and guiding filters with a varying central frequency. The physical parameter values are the same as in Fig. 21. The solid blue curve represents the result obtained by numerical simulations with Eq. (20). The red stars correspond to the prediction of the adiabatic perturbation theory, obtained with Eqs. (B3), (29), and (30).

and frequency dynamics along significantly larger distances compared with the distances obtained with the closed optical waveguide loop setups considered in sections III A and IV A. In this sense, stabilization of amplitude and frequency dynamics in waveguides with guiding filters with a varying central frequency is similar to the stabilization observed in Fig. 16, for waveguides with frequency dependent linear gain-loss, cubic loss, and delayed Raman response.

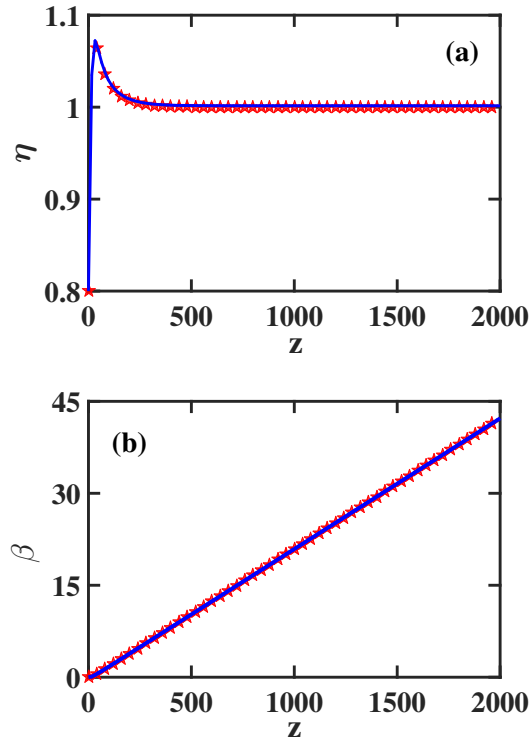


FIG. 24: The z dependence of the soliton amplitude $\eta(z)$ (a) and frequency $\beta(z)$ (b) for the closed optical waveguide loop setup considered in Figs. 21-23. The solid blue curves represent the results obtained by numerical simulations with Eq. (20). The red stars correspond to the predictions of the adiabatic perturbation theory, obtained with Eqs. (29) and (30).

V. CONCLUSIONS

We studied transmission stabilization against radiation emission for single-soliton propagation in nonlinear optical waveguides with weak linear gain-loss, cubic loss, and delayed Raman response. The value of the linear gain coefficient for waveguides with frequency independent linear gain was chosen such that stable soliton transmission with a constant amplitude can be realized. However, the presence of the linear gain can lead to an unstable growth of small amplitude waves (radiation) emitted by the soliton. We therefore looked for ways for stabilizing the transmission by frequency dependent linear gain-loss and delayed Raman response. We characterized transmission quality and stability by calculating the transmission quality integral, which measures the deviation of the pulse shape obtained in numerical simulations with perturbed NLS equations from the shape expected by the adiabatic perturbation theory for the NLS soliton. Additionally, we characterized stability of

amplitude and frequency dynamics by comparing the numerically obtained z dependence of the soliton's amplitude and frequency with the z dependence expected by the adiabatic perturbation theory.

We first studied soliton propagation in the absence of delayed Raman response. Our numerical simulations with the perturbed NLS propagation models showed that transmission quality in waveguides with frequency independent linear gain and cubic loss is comparable to transmission quality in waveguides with frequency dependent linear gain-loss and cubic loss. Furthermore, we found that in the absence of delayed Raman response, the presence of frequency dependent linear gain-loss does not lead to enhancement of transmission quality due to the lack of significant separation between the soliton's Fourier spectrum and the radiation's Fourier spectrum.

We then included the effects of delayed Raman response in the perturbed NLS model. Our numerical simulations showed that in waveguides with frequency independent linear gain, cubic loss, and delayed Raman response, the soliton's spectrum becomes separated from the radiation's spectrum due to the Raman self-frequency shift experienced by the soliton. However, in this case transmission quality was not improved compared with transmission quality in the absence of delayed Raman response due to the lack of an efficient mechanism for suppression of radiation emission. For the same reason, dynamics of the soliton's amplitude and frequency became unstable at intermediate propagation distances.

Drastic enhancement of transmission quality was demonstrated in waveguides with weak frequency dependent linear gain-loss, cubic loss, and delayed Raman response. In this case, our numerical simulations showed that the presence of delayed Raman response leads to separation of the soliton's spectrum from the radiation's spectrum, while the presence of frequency dependent linear gain-loss with relatively strong loss far from the soliton's frequency leads to efficient suppression of radiation emission. This enabled the observation of distortion-free soliton propagation and stable amplitude and frequency dynamics along significantly larger distances compared with the distances obtained in the absence of delayed Raman response and compared with the distances obtained in waveguides with frequency independent linear gain, cubic loss, and delayed Raman response. Further numerical simulations showed that enhancement of transmission quality in waveguides with weak frequency dependent linear gain-loss, cubic loss, and delayed Raman response is similar to transmission quality enhancement in waveguides with weak frequency independent linear gain, cubic

loss, and guiding filters with a varying central frequency. More specifically, the simulations demonstrated that the variation of the central filtering frequency leads to separation of the soliton's spectrum from the radiation's spectrum, while the presence of the guiding filters leads to efficient suppression of radiation emission.

Appendix A: The adiabatic perturbation theory for the fundamental NLS soliton

In this appendix we give a brief summary of the adiabatic perturbation theory for the fundamental NLS soliton, which was developed by Kaup [54, 55, 66]. The theory was used for analyzing soliton dynamics in a variety of optical waveguide systems, see, e.g., Refs. [3, 56] and references therein.

To illustrate the approach, consider the perturbed NLS equation

$$i\partial_z\psi + \partial_t^2\psi + 2|\psi|^2\psi = \epsilon h(t, z), \quad (\text{A1})$$

where $0 < |\epsilon| \ll 1$. We look for a solution of Eq. (A1) in the form:

$$\psi(t, z) = \psi_s(t, z) + \psi_{rad}(t, z) = \eta(z) \frac{\exp[i\chi(t, z)]}{\cosh(x)} + v(t, z) \exp[i\chi(t, z)], \quad (\text{A2})$$

where $x = \eta(z) [t - y(z)]$, $\chi(t, z) = \alpha(z) - \beta(z) [t - y(z)]$, $y(z) = y(0) - 2 \int_0^z dz' \beta(z')$, and $\alpha(z) = \alpha(0) + \int_0^z dz' [\eta^2(z') + \beta^2(z')]$. The first term on the right hand side of Eq. (A2) is the soliton solution with slow varying parameters, while the second term, which is of $O(\epsilon)$, is the radiation part. We now substitute Eq. (A2) into (A1) and keep terms up to $O(\epsilon)$. The resulting equation and its complex conjugate can be written in the following vector form:

$$\begin{aligned} & \frac{i}{\cosh(x)} \begin{pmatrix} 1 \\ -1 \end{pmatrix} \eta \left(\frac{d\alpha}{dz} + \beta \frac{dy}{dz} - \eta^2 + \beta^2 \right) + \frac{\tanh(x)}{\cosh(x)} \begin{pmatrix} 1 \\ 1 \end{pmatrix} \eta^2 \left(\frac{dy}{dz} + 2\beta \right) \\ & - \frac{ix}{\cosh(x)} \begin{pmatrix} 1 \\ -1 \end{pmatrix} \frac{d\beta}{dz} - \frac{[x \tanh(x) - 1]}{\cosh(x)} \begin{pmatrix} 1 \\ 1 \end{pmatrix} \frac{d\eta}{dz} + \partial_z \begin{pmatrix} v \\ v^* \end{pmatrix} - i\eta^2 \mathcal{L} \begin{pmatrix} v \\ v^* \end{pmatrix} \\ & - 2\beta \partial_t \begin{pmatrix} v \\ v^* \end{pmatrix} = -i\epsilon \begin{pmatrix} h(t, z)e^{-i\chi} \\ -h^*(t, z)e^{i\chi} \end{pmatrix}. \end{aligned} \quad (\text{A3})$$

The linear operator \mathcal{L} in Eq. (A3) is defined by:

$$\mathcal{L} = (\partial_x^2 - 1) \boldsymbol{\sigma}_3 + \frac{2}{\cosh^2(x)} (2\boldsymbol{\sigma}_3 + i\boldsymbol{\sigma}_2), \quad (\text{A4})$$

where $\boldsymbol{\sigma}_j$ with $1 \leq j \leq 3$ are the Pauli spin matrices.

The complete set of orthogonal eigenfunctions of \mathcal{L} was found in Refs. [54, 55, 66]. It includes four localized eigenfunctions, which appear in the first four terms on the left hand side of Eq. (A3):

$$\begin{aligned} f_0(x) &= \frac{1}{\cosh(x)} \begin{pmatrix} 1 \\ -1 \end{pmatrix}, & f_1(x) &= \frac{\tanh(x)}{\cosh(x)} \begin{pmatrix} 1 \\ 1 \end{pmatrix}, \\ f_2(x) &= \frac{x}{\cosh(x)} \begin{pmatrix} 1 \\ -1 \end{pmatrix}, & f_3(x) &= \frac{x \tanh(x) - 1}{\cosh(x)} \begin{pmatrix} 1 \\ 1 \end{pmatrix}. \end{aligned} \quad (\text{A5})$$

The eigenfunctions $f_0(x)$ and $f_1(x)$ have a zero eigenvalue, while $f_2(x)$ and $f_3(x)$ satisfy $\mathcal{L}f_2 = -2f_1$ and $\mathcal{L}f_3 = -2f_0$ [54, 55, 66]. The left localized eigenfunctions of \mathcal{L} , which are given by $f_m^T \boldsymbol{\sigma}_3$ for $0 \leq m \leq 3$, satisfy the following relations [54, 55, 66]:

$$\int_{-\infty}^{+\infty} dx f_2^T(x) \boldsymbol{\sigma}_3 f_1(x) = 2, \quad \int_{-\infty}^{+\infty} dx f_0^T(x) \boldsymbol{\sigma}_3 f_3(x) = -2. \quad (\text{A6})$$

In addition, the set of eigenfunctions of \mathcal{L} contains an infinite set of unlocalized eigenfunctions, which are characterized by a continuous index q , where $-\infty < q < \infty$. We obtain the dynamic equations for the four soliton parameters by projecting both sides of Eq. (A3) on the four left localized eigenfunctions of \mathcal{L} . In particular, the equations for amplitude and frequency dynamics are obtained by projecting both sides of Eq. (A3) on the left eigenfunctions $f_0^T(x) \boldsymbol{\sigma}_3 = \text{sech}(x)(1, 1)$ and $f_1^T(x) \boldsymbol{\sigma}_3 = \text{sech}(x) \tanh(x)(1, -1)$, respectively.

Appendix B: Calculation of the transmission quality integral $I(z)$

In this appendix we present the method used for calculating the transmission quality integral $I(z)$ and the transmission quality distance z_q from the results of the numerical simulations. In addition, we present the theoretical predictions for the soliton's shape and its Fourier transform, which were used in the analysis of transmission quality.

The theoretical prediction for the soliton's shape and the calculation of $I(z)$ are based on the adiabatic perturbation theory for the NLS soliton (see Refs. [3, 54–56] and A). According to the theory, the total optical field can be written as a sum of the soliton part ψ_s and the radiation part ψ_{rad} , where the soliton part is given by the expression for the soliton solution to the unperturbed NLS equation with slowly varying parameters [see Eq. (A2)]. We therefore take $\psi_s(t, z)$ as the theoretical prediction for the soliton part, i.e., $\psi^{(th)}(t, z) \equiv \psi_s(t, z) = \eta(z) \text{sech}(x) \exp(i\chi)$, where x and χ were defined in A. Therefore, the

theoretical prediction for the soliton's shape is given by

$$|\psi^{(th)}(t, z)| = \eta(z) \operatorname{sech} [\eta(z) (t - y(z))], \quad (\text{B1})$$

where $\eta(z)$ and $y(z)$ can be calculated by solving the equations for $d\eta/dz$ and dy/dz , which are obtained within the framework of the adiabatic perturbation theory. We point out that the value of $y(z)$ is not changed by linear gain-loss and by cubic loss. In addition, the value of $y(z)$ is affected by the Raman perturbation in first-order in ϵ_R only via the z dependence of the soliton's frequency. Therefore, in the current paper, we calculate the value of $\eta(z)$ in Eq. (B1) by solving the perturbation theory's equation for $d\eta/dz$, while the value of $y(z)$ is measured from the results of the numerical simulations. The Fourier transform of $\psi_s(t, z)$ with respect to time is

$$\hat{\psi}_s(\omega, z) = \left(\frac{\pi}{2}\right)^{1/2} \frac{\exp[i\alpha(z) - i\omega y(z)]}{\cosh [\pi (\omega + \beta(z)) / (2\eta(z))]} . \quad (\text{B2})$$

Thus, the theoretical prediction for the Fourier transform of the soliton's shape is given by:

$$|\hat{\psi}^{(th)}(\omega, z)| = \left(\frac{\pi}{2}\right)^{1/2} \operatorname{sech} [\pi (\omega + \beta(z)) / (2\eta(z))], \quad (\text{B3})$$

where $\eta(z)$ and $\beta(z)$ are calculated by solving the equations for $d\eta/dz$ and $d\beta/dz$ that are obtained with the adiabatic perturbation theory.

The transmission quality integral $I(z)$ measures the deviation of the pulse shape obtained in the numerical simulations $|\psi^{(num)}(t, z)|$ from the soliton's shape predicted by the adiabatic perturbation theory $|\psi^{(th)}(t, z)|$. We use the same definition of $I(z)$ that was used in Ref. [16] for characterizing transmission stability in multisequence soliton-based optical waveguide systems. Thus, $I(z)$ is defined by the relation

$$I(z) = \tilde{I}^{(dif)}(z) / \tilde{I}(z), \quad (\text{B4})$$

where $\tilde{I}^{(dif)}(z)$ and $\tilde{I}(z)$ are defined by

$$\tilde{I}^{(dif)}(z) = \left\{ \int_{t_{min}}^{t_{max}} dt [|\psi^{(th)}(t, z)| - |\psi^{(num)}(t, z)|]^2 \right\}^{1/2}, \quad (\text{B5})$$

and

$$\tilde{I}(z) = \left[\int_{t_{min}}^{t_{max}} dt |\psi^{(th)}(t, z)|^2 \right]^{1/2}. \quad (\text{B6})$$

From this definition it is clear that $I(z)$ measures both distortion in the pulse shape due to radiation emission and deviations of the numerically obtained values of the soliton's parameters from the values predicted by the adiabatic perturbation theory. The transmission quality distance z_q is defined as the distance at which the value of $I(z)$ first exceeds a constant value C . In the current paper we used $C = 0.075$. We emphasize, however, that the values of the transmission quality distance obtained by using this definition are not very sensitive to the value of the constant C . That is, we found that small changes in the value of C lead to small changes in the measured z_q values.

Appendix C: Amplitude dynamics in the presence of frequency dependent linear gain-loss

In the current appendix we derive Eq. (9) for the dynamics of the soliton's amplitude in waveguides with frequency dependent linear gain-loss and cubic loss. The calculation of the effects of cubic loss on amplitude dynamics is straightforward and has been presented in earlier works (see, e.g., Refs. [12, 29]). We therefore concentrate mainly on calculating the effects of frequency dependent linear gain-loss on amplitude dynamics.

We introduce the following notations for the two perturbation terms on the right hand side of Eq. (6): $h_1(t, z) = i\mathcal{F}^{-1}(\hat{g}(\omega)\hat{\psi})/2$ and $h_2(t, z) = -i\epsilon_3|\psi|^2\psi$, and assume that $\hat{g}(\omega)$ can be approximated by Eq. (8). In the leading order of the perturbation theory, we approximate ψ and $\hat{\psi}$ by the soliton parts ψ_s and $\hat{\psi}_s$, which are given by Eqs. (A2) and (B2), respectively. Therefore [67]:

$$h_1(t, z) \simeq i\mathcal{F}^{-1}(\hat{g}(\omega)\hat{\psi}_s)/2, \quad (\text{C1})$$

and

$$h_2(t, z) \simeq -i\epsilon_3|\psi_s|^2\psi_s. \quad (\text{C2})$$

We first calculate the contribution of $h_1(t, z)$ to the right hand side of Eq. (9). Using the convolution theorem, we obtain:

$$\mathcal{F}^{-1}(\hat{g}(\omega)\hat{\psi}_s) = (2\pi)^{-1/2} \int_{-\infty}^{\infty} ds g(s)\psi_s(t-s, z). \quad (\text{C3})$$

Calculation of the inverse Fourier transform of $\hat{g}(\omega)$ yields

$$g(t) = -(2\pi)^{1/2}g_L\delta(t) + \left(\frac{2}{\pi}\right)^{1/2} (g_0 + g_L) \exp[-i\beta(0)t] \sin(Wt/2)/t, \quad (\text{C4})$$

where $\delta(t)$ is the Dirac delta function. Substituting Eq. (C4) into Eq. (C3) while using the expression for $\psi_s(t, z)$ in Eq. (A2), we obtain the following equation for the leading order approximation for $-ih_1(t, z)$:

$$-ih_1(t, z) \simeq \frac{-g_L \eta e^{ix}}{2 \cosh(x)} + \frac{(g_0 + g_L)}{2\pi} \eta e^{ix} \int_{-\infty}^{\infty} ds \frac{\sin(Ws/2)}{s \cosh(x - \eta s)}. \quad (\text{C5})$$

From Eq. (C5) it follows that

$$-i \begin{pmatrix} h_1(t, z) e^{-ix} \\ -h_1^*(t, z) e^{ix} \end{pmatrix} \simeq \frac{-g_L \eta}{2 \cosh(x)} \begin{pmatrix} 1 \\ 1 \end{pmatrix} + \frac{(g_0 + g_L)}{2\pi} \eta \begin{pmatrix} 1 \\ 1 \end{pmatrix} \int_{-\infty}^{\infty} ds \frac{\sin(Ws/2)}{s \cosh(x - \eta s)}. \quad (\text{C6})$$

A straightforward calculation for the contribution of the cubic loss term yields:

$$-i \begin{pmatrix} h_2(t, z) e^{-ix} \\ -h_2^*(t, z) e^{ix} \end{pmatrix} \simeq -\frac{\epsilon_3 \eta^3}{\cosh^3(x)} \begin{pmatrix} 1 \\ 1 \end{pmatrix}. \quad (\text{C7})$$

Substituting Eqs. (C6) and (C7) into Eq. (A3) and projecting both sides of the resulting equation on the left eigenfunction $f_0^T(x) \boldsymbol{\sigma}_3 = \text{sech}(x)(1, 1)$ of the linear operator \mathcal{L} , we obtain:

$$\frac{d\eta}{dz} = \left[-g_L + (g_0 + g_L) \tilde{J}(\eta; W)/(2\pi) - 4\epsilon_3 \eta^2/3 \right] \eta. \quad (\text{C8})$$

The function $\tilde{J}(\eta; W)$ in Eq. (C8) is given by:

$$\begin{aligned} \tilde{J}(\eta; W) &= \int_{-\infty}^{\infty} ds \frac{\sin(Ws/2)}{s} \int_{-\infty}^{\infty} \frac{dx}{\cosh(x) \cosh(x - \eta s)} \\ &= 2\pi \text{sgn}(\eta) \tanh\left(\frac{\pi W}{4\eta}\right) \end{aligned} \quad (\text{C9})$$

for $\eta \neq 0$, where $W > 0$ is used [67]. Substituting Eq. (C9) into Eq. (C8) and using the notation $V = \pi W/(4\eta)$, we obtain [68]:

$$\frac{d\eta}{dz} = \left[-g_L + (g_0 + g_L) \text{sgn}(\eta) \tanh(V) - 4\epsilon_3 \eta^2/3 \right] \eta. \quad (\text{C10})$$

Since in the physical problem $\eta \geq 0$, we arrive at:

$$\frac{d\eta}{dz} = \left[-g_L + (g_0 + g_L) \tanh(V) - 4\epsilon_3 \eta^2/3 \right] \eta, \quad (\text{C11})$$

which is Eq. (9).

We now discuss stability properties of the equilibrium points $\eta = \eta_0$ and $\eta = 0$ of Eq. (11). Stability of the equilibrium point $\eta = 0$ is established in a more convenient manner with the

help of Eq. (C10). We therefore use Eq. (C10) in the following analysis. Substituting Eq. (10) for g_0 into Eq. (C10), we obtain:

$$\frac{d\eta}{dz} = \eta \left\{ g_L \left[\frac{\text{sgn}(\eta) \tanh(V)}{\tanh(V_0)} - 1 \right] + \frac{4}{3} \epsilon_3 \left[\eta_0^2 \frac{\text{sgn}(\eta) \tanh(V)}{\tanh(V_0)} - \eta^2 \right] \right\}. \quad (\text{C12})$$

Denote the right hand side of Eq. (C12) by $H(\eta)$. It is straightforward to show that $H(\eta) < 0$ for $\eta > \eta_0$, $H(\eta) > 0$ for $0 < \eta < \eta_0$, and $H(\eta) < 0$ for $-\eta_0 < \eta < 0$. It follows that there are no additional equilibrium points with $\eta > 0$, and that $\eta = \eta_0$ is a stable equilibrium point, while $\eta = 0$ is an unstable equilibrium point. Thus, the number, locations, and stability properties of the equilibrium points of Eq. (11) and Eq. (4) are the same.

Acknowledgments

D.C. is grateful to the Mathematics Department of NJCU for providing technological support for the computations.

References

-
- [1] G.P. Agrawal, *Nonlinear Fiber Optics*, Academic, San Diego, CA, 2001.
 - [2] L.F. Mollenauer and J.P. Gordon, *Solitons in Optical Fibers: Fundamentals and Applications*, Academic, San Diego, CA, 2006.
 - [3] A. Hasegawa and Y. Kodama, *Solitons in Optical Communications*, Clarendon, Oxford, 1995.
 - [4] E. Iannone, F. Matera, A. Mecozzi, and M. Settembre, *Nonlinear Optical Communication Networks*, Wiley, New York, 1998.
 - [5] L.F. Mollenauer, J.P. Gordon, and P.V. Mamyshev, in: I.P. Kaminow and T.L. Koch (Eds.), *Optical Fiber Telecommunications III*, Academic, San Diego, CA, 1997, Chapter 12.
 - [6] L.F. Mollenauer and P.V. Mamyshev, *IEEE J. Quantum Electron.* **34**, 2089 (1998).
 - [7] M. Nakazawa, *IEEE J. Sel. Top. Quantum Electron.* **6**, 1332 (2000).
 - [8] M. Nakazawa, E. Yamada, H. Kubota, and K. Suzuki, *Electron. Lett.* **27**, 1270 (1991).
 - [9] L.F. Mollenauer, P.V. Mamyshev, and M.J. Neubelt, *Electron. Lett.* **32**, 471 (1996).
 - [10] L.F. Mollenauer, A. Grant, X. Liu, X. Wei, C. Xie, and I. Kang, *Opt. Lett.* **28**, 2043 (2003).

- [11] Q.M. Nguyen and A. Peleg, *Opt. Commun.* **283**, 3500 (2010).
- [12] A. Peleg, Q.M. Nguyen, and Y. Chung, *Phys. Rev. A* **82**, 053830 (2010).
- [13] A. Peleg and Y. Chung, *Phys. Rev. A* **85**, 063828 (2012).
- [14] D. Chakraborty, A. Peleg, and J.-H. Jung, *Phys. Rev. A* **88**, 023845 (2013).
- [15] Q.M. Nguyen, A. Peleg, and T.P. Tran, *Phys. Rev. A* **91**, 013839 (2015).
- [16] A. Peleg, Q.M. Nguyen, and T.P. Tran, *Opt. Commun.* **380**, 41 (2016).
- [17] A. Peleg, Q.M. Nguyen, and T.T. Huynh, *Eur. Phys. J. D* **71**, 30 (2017).
- [18] A. Peleg and D. Chakraborty, “Large stable oscillations due to Hopf bifurcations in amplitude dynamics of colliding soliton sequences”, *Commun. Nonlinear Sci. Numer. Simulat.*, in press, arXiv:1612.03429.
- [19] D. Chakraborty, A. Peleg, and Q.M. Nguyen, *Opt. Commun.* **371**, 252 (2016).
- [20] F.M. Mitschke and L.F. Mollenauer, *Opt. Lett.* **11**, 659 (1986).
- [21] J.P. Gordon, *Opt. Lett.* **11**, 662 (1986).
- [22] Y. Kodama and A. Hasegawa, *IEEE J. Quantum Electron.* **23**, 510 (1987).
- [23] R.W. Boyd, *Nonlinear Optics*, Academic, San Diego, CA, 2008.
- [24] Q. Lin, O.J. Painter, and G.P. Agrawal, *Opt. Express* **15**, 16604 (2007).
- [25] R. Dekker, N. Usechak, M. Först, and A. Driessen, *J. Phys. D* **40**, R249 (2007).
- [26] G.S. He, L.-S. Tan, Q. Zheng, and P.N. Prasad, *Chem. Rev.* **108**, 1245 (2008).
- [27] Y.S. Kivshar and B.A. Malomed, *Rev. Mod. Phys.* **61**, 763 (1989).
- [28] V. Mizrahi, K.W. DeLong, G.I. Stegeman, M.A. Saifi, and M.J. Andrejco, *Opt. Lett.* **14**, 1140 (1989).
- [29] Y. Silberberg, *Opt. Lett.* **15**, 1005 (1990).
- [30] A.B. Aceves and J.V. Moloney, *Opt. Lett.* **17**, 1488 (1992).
- [31] G.S. He, J.D. Bhawalkar, C.F. Zhao, and P.N. Prasad, *Appl. Phys. Lett.* **67**, 2433 (1995).
- [32] V.V. Afanasjev, J.S. Aitchison, and Y.S. Kivshar, *Opt. Commun.* **116**, 331 (1995).
- [33] E.N. Tsoy, C.M. de Sterke, and F.Kh. Abdullaev, *J. Opt. Soc. Am. B* **18**, 1144 (2001).
- [34] O. Katz, Y. Lahini, and Y. Silberberg, *Opt. Lett.* **33**, 2830 (2008).
- [35] A. Peleg, Y. Chung, T. Dohnal, and Q.M. Nguyen, *Phys. Rev. E* **80**, 026602 (2009).
- [36] Y. Okawachi, O. Kuzucu, M.A. Foster, R. Salem, A.C. Turner-Foster, A. Biberman, N. Ophir, K. Bergman, M. Lipson, and A.L. Gaeta, *IEEE Photon. Technol. Lett.* **24**, 185 (2012).
- [37] M.A. Foster, A.C. Turner, M. Lipson, and A.L. Gaeta, *Opt. Express* **16**, 1300 (2008).

- [38] R. Soref, IEEE J. Sel. Top. Quantum Electron. **12**, 1678 (2006).
- [39] R. Jones, A. Liu, H. Rong, M. Paniccia, O. Cohen, and D. Hak, Opt. Express **13**, 1716 (2005).
- [40] S.F. Preble, Q. Xu, B.S. Schmidt, and M. Lipson, Opt. Lett. **30**, 2891 (2005).
- [41] Ö. Boyraz, P. Koonath, V. Raghunathan, and B. Jalali, Opt. Express **12**, 4094 (2004).
- [42] T.K. Liang, L.R. Nunes, T. Sakamoto, K. Sasagawa, T. Kawanishi, M. Tsuchiya, G.R.A. Priem, D. Van Thourhout, P. Dumon, R. Baets, and H.K. Tsang, Opt. Express **13**, 7298 (2005).
- [43] R. Salem, M.A. Foster, A.C. Turner, D.F. Geraghty, M. Lipson, and A.L. Gaeta, Opt. Express **15**, 7802 (2007).
- [44] E. Tien, N.S. Yuksek, F. Qian, and O. Boyraz, Opt. Express **15**, 6500 (2007).
- [45] T.K. Liang, L.R. Nunes, M. Tsuchiya, K.S. Abedin, T. Miyazaki, D. Van Thourhout, W. Bogaerts, P. Dumon, R. Baets, and H.K. Tsang, Opt. Commun. **265**, 171 (2006).
- [46] M. Xiong, L. Lei, Y. Ding, B. Huang, H. Ou, C. Peucheret, and X. Zhang, Opt. Express **21**, 25772 (2013).
- [47] L. Yin, Q. Lin, and G. P. Agrawal, Opt. Lett. **32**, 391 (2007).
- [48] M.N. Islam (Ed.), Raman Amplifiers for Telecommunications 1: Physical Principles, Springer, New York, 2004.
- [49] C. Headley and G.P. Agrawal (Eds.), Raman Amplification in Fiber Optical Communication Systems, Elsevier, San Diego, CA, 2005.
- [50] R. Claps, D. Dimitropoulos, V. Raghunathan, Y. Han, and B. Jalali, Opt. Express **11**, 1731 (2003).
- [51] Q. Xu, V.R. Almeida, and M. Lipson, Opt. Express **12**, 4437 (2004).
- [52] R. Jones, H. Rong, A. Liu, A. Fang, M. Paniccia, D. Hak, and O. Cohen, Opt. Express **13**, 519 (2005)
- [53] The dimensionless distance z in Eq. (1) is $z = X/(2L_D)$, where X is the dimensional distance, $L_D = \tau_0^2/|\tilde{\beta}_2|$ is the dispersion length, τ_0 is the soliton width, and $\tilde{\beta}_2$ is the second-order dispersion coefficient. The dimensionless time is $t = \tau/\tau_0$, where τ is time. $\psi = (\gamma\tau_0^2/|\tilde{\beta}_2|)^{1/2}E$, where E is the electric field and γ is the Kerr nonlinearity coefficient. The coefficients g_0 and ϵ_3 are related to the dimensional linear gain and cubic loss coefficients ρ_1 and ρ_3 by $g_0 = 2\tau_0^2\rho_1/|\tilde{\beta}_2|$ and $\epsilon_3 = 2\rho_3/\gamma$.
- [54] D.J. Kaup, Phys. Rev. A **42**, 5689 (1990).

- [55] D.J. Kaup, Phys. Rev. A **44**, 4582 (1991).
- [56] M. Chertkov, Y. Chung, A. Dyachenko, I. Gabitov, I. Kolokolov, and V. Lebedev, Phys. Rev. E **67**, 036615 (2003).
- [57] J. Yang, Nonlinear Waves in Integrable and Nonintegrable Systems, SIAM, Philadelphia, 2010.
- [58] E.A. Kuznetsov, A.V. Mikhailov, and I.A. Shimokhin, Physica D **87**, 201 (1995).
- [59] J. Soneson and A. Peleg, Physica D **195**, 123 (2004).
- [60] P.C. Becker, N.A. Olsson, and J.R. Simpson, Erbium-Doped Fiber Amplifiers: Fundamentals and Technology, Academic, San Diego, CA, 1999, chapter 8.
- [61] This setup corresponds to the one used in many soliton-based transmission experiments, where the pulses propagate with a prescribed peak power and the frequency difference between adjacent pulse sequences is much larger than the spectral width of the pulses [1, 6, 7].
- [62] The dimensionless Raman coefficient ϵ_R in Eq. (13) is $\epsilon_R = 2\tau_R/\tau_0$, where τ_R is a dimensional time constant, characterizing the nonlinear waveguide's delayed Raman response [1, 63]. The time constant τ_R can be determined from the slope of the Raman gain curve of the waveguide [1, 63].
- [63] S. Chi and S. Wen, Opt. Lett. **14**, 1216 (1989).
- [64] L.F. Mollenauer, J.P. Gordon, and S.G. Evangelides, Opt. Lett. **17**, 1575 (1992).
- [65] The dimensionless second-order filtering coefficient ϵ_ω in Eq. (19) is $\epsilon_\omega = 2\tilde{\epsilon}_\omega/|\tilde{\beta}_2|$, where $\tilde{\epsilon}_\omega$ is the dimensional second-order filtering coefficient. The dimensionless central filtering frequency is $\omega_p = \tilde{\omega}_p\tau_0$, where $\tilde{\omega}_p$ is the dimensional central filtering frequency.
- [66] D.J. Kaup, J. Math. Anal. Appl. **54**, 849 (1976).
- [67] Note that for $\eta(z) = 0$, $\psi_s(t, z) \equiv 0$ and $\hat{\psi}_s(\omega, z) \equiv 0$. Therefore, in this case, $h_1(t, z) = 0$ and $d\eta/dz = 0$ in the leading order of the perturbation theory.
- [68] Note that similar to the right hand side of Eq. (3), the right hand side of Eq. (C10) is a continuous function of η for any η , including $\eta = 0$. Additionally, the right hand side of Eq. (C10) tends to 0 as η tends to 0, in accordance with the statements in Ref. [67].